Characterization of a setup for broadband signal recordings in an MRI environment

Final Research Paper

zur Erlangung des

MARSHALL PLAN
SCHOLARSHIP

Eingereicht bei

Austrian Marshall Plan
Foundation

von

Astrid Höllinger

Linz, am 22.06.2018

Eidesstattliche Erklärung

Ich erkläre eidesstattlich, dass ich die vorliegende Arbeit selbstständig und ohne fremde Hilfe verfasst, andere als die angegebenen Quellen nicht benutzt und die den benutzten Quellen entnommenen Stellen als solche gekennzeichnet habe. Die Arbeit wurde bisher in gleicher oder ähnlicher Form keiner anderen Prüfungsbehörde vorgelegt.

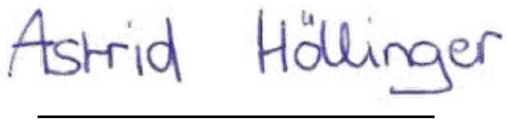

Linz, am 22.06.2018

Astrid Höllinger

Declaration

I hereby declare and confirm that this thesis is entirely the result of my own original work. Where other sources of information have been used, they have been indicated as such and properly acknowledged. I further declare that this or similar work has not been submitted for credit elsewhere.

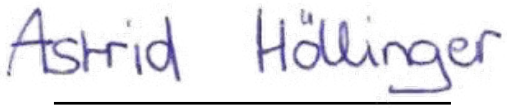

Linz, 22.06.2018

Astrid Höllinger

Acknowledgements

I am deeply grateful for the continuous assistance, support and valuable contributions of numerous people to this thesis - I want to thank all of you, without you it would not have been possible!

Firstly, I would like to express my sincere gratitude to my supervisor at the University of Applied Sciences Upper Austria, FH-Prof. PD Dr. Thomas Haslwanter for the kind support, critical considerations and helpful advices. Thank you for giving me the freedom to work independently and the many possibilities to realize my own ideas, while at the same time always guiding me in the right direction at critical points.

Besides my wise mentor and advisor, I want to say thank you to the team of the Laboratory of Neural Systems at the Rockefeller University in New York. Thank you for your warm reception, it was a great pleasure and privilege for me to be part of this wonderful research group for half of a year.

In particular, I want to express my gratitude to the Head of the Laboratory Winrich Freiwald, Ph.D. Thank you for providing me the possibility to work in one of the best work atmospheres to conduct research for the following thesis. Thank you for your valuable comments and encouragement, but also for the continuous questioning of my work which made me look at my research from new perspectives.

Furthermore, I want to say thank you to my first contact person in the laboratory, Zetian Yang. Thank you for being a very helpful mentor and advisor in every single step during the development of this thesis. I want to acknowledge you for always having an open ear for me during the whole project. Also, I want to thank all other lab members for every interesting talk and discussion and all the fun we had together.

Then, I want to acknowledge the whole team of the Weill Cornell Medical College. Especially, I want to thank Muc Chieu Du for being a supportive and always helpful laboratory administrator and Jonathan Dyke for the technical assistance on the MRI scanner.

Also, I would like to thank David Leopold, Ph.D., Senior Investigator at the National Institute of Mental Health in Washington, D.C. Thank you for always having an open ear for me despite your very busy job position and all your support in regard with setting up the Tucker Davis system in an MRI environment.

Last but not least, I would like to acknowledge my friends and family who supported me during my exchange semester in New York and in general throughout my studies in Linz. Especially, I want to thank my parents and my brother for your loving support and the encouragement.

Kurzfassung

Die simultane Aufnahme von elektrophysiologischen Messungen und funktioneller Bildgebung erlaubt es das maximale Potential beider Technologien für die Untersuchung von neuronalen Ereignissen zu vereinen. Die funktionelle Magnetresonanztomographie hat sich heute zur der am häufigsten verwendeten Methode zur Untersuchung von Hirnaktivität und funktionellen neurologischen Netzwerken etabliert. Die zeitliche Auflösung der Technologie ist jedoch limitiert und daher bleibt die exakte neurologische Aktivität unbekannt. Mithilfe elektrophyisologischer Ableitungen lassen sich hohe zeitliche Auflösungen erreichen. Die Methode erlaubt es die physiologischen Eigenschaften von Zellen oder Populationen von Zellen genau zu studieren. Durch die simultane Verwendung beider Technologien könnte es in naher Zukunft zu entscheidenden neuen Erkenntnissen im Bereich der Hirnforschung kommen. Jedoch ist diese Kombination mit sehr hohen Herausforderungen verbunden, da die gemessenen Signale im Bereich von nur wenigen µV liegen. Unerwünschte Wechselwirkungen können zur Verminderung der Signalqualität oder im schlimmsten Fall zur Schädigung des technischen Equipments führen. In der vorliegenden Arbeit wird ein elektrophysiologisches Setup zur Verwendung im Magnetresonanztomographen entwickelt und getestet. Das besondere Augenmerk liegt in den Herausforderungen, die sich ergeben durch die simultane Verwendung im Magnetfeld. Außerdem wird ein Mikrostimulationssetup zur künstlichen Anregung von bestimmten Hirnarealen aufgebaut und getestet.

Abstract

The simultaneous recording of electrophysiological signals and functional magnetic resonance imaging makes it possible to combine the maximal potential of both technologies for the investigation of neuronal events. Functional magnetic resonance imaging is nowadays the most widely used technology for mapping brain activation and study of functional neural networks. However, the temporal resolution of the method is limited and thus the exact underlying neural activity often remains unknown. Electrophysiological recordings are the method of choice to achieve high temporal resolutions on a cellular and even sub-cellular scale. The method makes it possible to investigate physiological properties of single cells or a cluster of them. The simultaneous use of both technologies might contribute to new valuable insights in modern brain research in the near future. However, this combination rises several challenges as the measured signals typically lie in the range of only several µV. Undesired interference can lead to a decrease in signal quality or even in damage of the equipment. In the following work a setup for electrophysiological recordings in a magnetic resonance imaging environment is developed and characterized. A focus is on the challenges that arise from the simultaneous use of the setup in the magnetic field. Furthermore, a microstimulation setup is developed and tested for the artificial stimulation of a specific brain area.

Executive Summary

An upcoming research topic in the study of brain activity is the simultaneous recording of electrophysiological signals and functional magnetic resonance imaging. This promising combination enables us to assure the full potential of both technologies. Functional magnetic resonance imaging has been developed to the most widely used technology for mapping brain activity and studying functional neural networks nowadays. However, the exact relationship between the measured functional magnetic resonance imaging signal and the underlying neural activity is complex and often unknown. Electrophysiological recordings, i.e. the low frequency local field potentials superimposed on high frequency spike activity of single cells or a cluster of them, enables the study of physiological properties with an excellent temporal resolution on a cellular and sub-cellular scale. In recent years electrophysiological recordings found application in animal research where electrophysiological recordings are performed extracellular with electrodes in the brain region of interest. However, the simultaneous use of both methodologies rises high challenges as the measured neural signals lie in the range of only several µV. Signal quality decreases or damage of the equipment due to undesired interference are likely and often inevitable in the worst case.

In the following work a setup for electrophysiological recordings in an MRI environment is developed and characterized. Initially, various systems from different vendors are setup and evaluated in regard to their suitability for an extension to an fMRI compatible version. After a decision is made for the further use of the Tucker Davis system, the same is tested in the laboratory setting, in the static magnetic field of an MRI scanner and during fMRI. Two different signal sources are applied for testing, i.e. a function generator and a resistor simulating properties of brain tissue. The Tucker Davis system is successfully tested in the MRI environment. It is found that the static magnetic field causes distortion in the low frequency range of the recorded broadband signal. The exact cause for a specific frequency noise peak in the amplitude spectrum is hard to determine as several factors, i.e. scanner noise can lead to an undesired distortion. However, broadband unspecific frequency noise starting at 20 Hz to 30 Hz with the most pronounced amplitude power between 50 Hz to 100 Hz is found to be mainly caused by the helium pump system. Sharp noise amplitude peaks are identified at 41 Hz and 43 Hz across different setup configurations and measurements. The scanner's internal ventilation system is suspected to be responsible for those frequency noise peaks. In addition, unstable and unspecific noise is found in the low frequency range $<$1000 Hz whose sources remain unknown. Possible causes are variations in the loop area, movement of equipment, interference with additional electrical devices in the scanner room, e.g. lights, monitors, etc. As the recorded signals are only in the range of µV a distortion induced by the magnetic field is often by magnitudes higher than the desired signal. Therefore it is assumed that noise reduction strategies in the setting up phase are very crucial for a good signal quality. The most prominent noise source are the switching readout gradients applied during functional imaging. In one of the two tested setup configurations, the fast polarity change of the readout gradients even causes saturation of the pre-amplifier and thus makes the post-hoc removal of

the artefact impossible. However, in the setup testing with the resistor as signal source the pre-amplifier is not saturated. Thus, the recording data could be cleared with several artefact removal strategies described elsewhere. To sum up, the testing of the Tucker Davis equipment in this study is successful. It could be shown that the system works according to its specifications and the raw data results can be explained for the most part with literature. So, nothing should affect the further conduction of measurements and more precise characterization in quantity, shape and stability of the recorded data. In a next step artefact removal strategies can be developed and then the setup should be able to be used in animal research studies.

Additionally, a microstimulation setup is developed and tested for the artificial activation of a specific brain area. The testing of the device in the laboratory setting is successful. It is found that the stimulus current at the brain region is diminished by around 50 % compared to its original value. The shape of the current is also varied due to capacitive properties of the cables. Thus, the following setup can also be used in animal studies, i.e. for the research on facial expression.

Abbreviations

AC	Alternating current
BOLD	Blood oxygenation level-dependent
CH	Channel
DC	Direct current
DSP	Digital signal processing
ECG	Electrocardiogram
EEG	Electroencephalography
EMF	Electromotive force
EPI	Echo-planar imaging
FFT	Fast Fourier transform
fMRI	Functional magnetic resonance imaging
FOV	Field of view
FPGA	Field-programmable gate array
GND	Ground
GUI	Graphical user interface
I/O	Input / Output
LFP	Local field potential
MRI	Magnetic resonance imaging
PC	Personal computer
PCA	Principal component analysis
PCI	Peripheral Component Interconnect
RF	Radio frequency
RMS	Root-mean square
scope	Oscilloscope
SPI	Serial Peripheral Interface
SNR	Signal-to-noise ratio
TDT	Tucker Davis Technologies

TE	Echo time
TR	Repetition time
USB	Universal Serial Bus

Contents

1 Introduction

In this chapter the problem this paper is associated with is outlined in Section 1.1. Additionally, the goals, sub-goals and also non-goals are precisely formulated in Section 1.2. Finally, the main contents of the chapters this thesis is composed of and how they are connected with each other are given in Section 1.3.

1.1 Problem statement

Since its introduction in the 1990s functional magnetic resonance imaging (fMRI) has rapidly developed to the most important noninvasive imaging tool for the study of brain activation nowadays. In short, it is based on the detection of changes in oxygenation, blood volume and flow following an increased neural activity in a specific brain region. This can be explained by the following: During the execution of behavioral and cognitive tasks some regions of the brain get more activated than others due to increased blood flow and volume and subsequently the oxygen saturation of the blood in the specific brain region increases. This localized higher amount of oxygen results in a variation of the magnetic properties of the brain tissue which further causes a variation that can be detected in the magnetic field of an MRI scanner. Although fMRI can provide very good spatial resolution, the temporal resolution is limited due to the delayed blood oxygen level rise and peak triggered by neural activation. This significant disadvantage gave reason to combine the technology with other complementary methodologies to study the brain's activity. Initially, several research groups combined the technology with EEG, i.e. electrical currents generated from the almost synchronous firing of a large amount of neurons, recorded on the scalp surface, and optical imaging. Although, new insights in brain functions could thus be gained and a lot of widespread application fields developed, i.e. the first and most important application of EEG-fMRI is in the epilepsy study, there still remained unsolved issues. Unfortunately, none of them were successful in the determination of the exact correlation between the measured fMRI signal and the actual underlying neural activity so far. One established method to examine neural activity including spatial distributed fast-varying action potentials superimposed with slow-varying field potentials are extracellular electrophysiological recordings with microelectrodes in the nonhuman brain. The simultaneous use of both technologies is a very challenging task and has only been tried by very few research groups worldwide. This thesis now tries to add a valuable contribution to this novel, challenging research topic by developing and characterizing a fully fMRI compatible extracellular electrophysiological setup [12, 28, 34].

As mentioned above fMRI is able to detect task-induced active brain states. Another possibility to artificially stimulate a specific brain region is via microstimulation electrodes in the nonhuman brain. Thus, another focus lies on the development

and characterization of a microstimulation setup in a laboratory setting in this thesis.

1.2 Goals and non-goals

As mentioned above the simultaneous use of extracellular electrophysiological recordings with microelectrodes in the nonhuman brain and fMRI is a very challenging task which is only studied by a few research groups worldwide. A complete coverage of the whole topic is of course not possible and would go beyond the scope of this paper. Thus, this thesis focuses only on parts of this very complex topic which are described in more detail in the following.

One aim of this thesis is to give the reader an introduction and the general motivation for the combination of both methodologies. Furthermore, both the origin and characteristics of the fMRI and the electrophysiological signal including single cell activity superimposed with slow-varying local field potentials, relevant for their combination, are outlined. However, a complete description of the physics of MRI and the thus developed functional MRI would exceed the scope of this thesis. For more details, the interesting reader is directed to various excellent papers (see [16] and [57]). The physiology of neural activity is complex and not part of this thesis. For a detailed description of physiological properties of individual neural cells and signal transmission, comprehensive descriptions are available elsewhere (see [24]).

The major goal of this thesis is to show the reader the challenges associated with the combination of both technologies. As this research topic is very new and rarely studied, literature review is based on the combination of EEG-fMRI assuming that occurring issues are similar. However, it was kept in mind that the combination of extracellular microelectrode electrophysiological recordings and fMRI are aggravating the problems in respect to the instrumentation. While EEG recordings are only in the low-frequency domain and amplitudes are limited to several µV, LFPs and action potentials measured directly in the extracellular space show much higher amplitudes and a broader frequency range. Thus, demands on technical equipment inside the scanner environment increase. Challenges are outlined connected to the stage of data acquisition and mainly related with artefacts occurring due to the scanner environment. Note that the list of artefacts provided within this thesis is based on literature review on EEG-fMRI and was created with the best of knowledge and conscience but cannot be guaranteed of completion as scanner environments, instrumentation, etc. vary among different research groups. Challenges are connected to distortion of the electrophysiological data due to an MRI environment and the execution of functional MRI. Problems connected to distortion of fMRI images and patient's safety are not part of this paper. Issues and problems that arise from the post-processing of the data, i.e. artefact removal strategies are only mentioned, but not further described within this thesis. It is not topic of the paper to show and explain detailed artefact removal strategies. Based on the challenges mentioned, the thesis outlines recommendations for an optimized setup instrumentation configuration within the MRI environment. Note that these recommendations do not include optimization steps including parameter settings of the instrumentation equipment which are further necessary for the artefact removal strategies.

Another sub-goal of this thesis is to show the reader already implemented applications of EEG-fMRI, their limitation and the resulting motivation for extracellular electrophyisological recordings and fMRI. Moreover, the thesis shows current ongoing research work on simultaneous recording of extracellular electrophysiological signals and functional imaging in nonhuman primates.

The following thesis wants to outline a general introduction and motivation for electrical microstimulation in nonhuman primates. Currently the main focus of research in nonhuman primates is also outlined.

In the practical part of the paper the main goal is the development and subsequent technical characterization of a setup for broadband signal recordings in the magnetic field of MRI scanners. Initially, various setups for broadband signal recordings are tested in a typical laboratory setting and then evaluated with respect to their suitability in an MRI environment. Based on the results of this comparison, a decision is made on the Tucker Davis system for the further testing in an MRI scanner. Signal recordings are conducted in the natural environment, the static magnetic field and during an fMRI scan with the system. The main aim is the characterization of artefacts with respect to its origin, quantity, shape and stability.

The second sub-goal is to develop and characterize a setup for microstimulation for the use in an MRI scanner. Here, the characterization is only done in a laboratory setting. Thus, the goal is to define if the setup works according to its specifications and if it is possible to use the same at a later time in an MRI environment for animal studies. It is not topic of the thesis to outline challenges or issues arising from the use of the setup in an MRI environment.

It is not goal of the paper to use any of the setups for animal research. As both technologies are still in its infancy, a detailed technical characterization of both is far more important than any precipitant studies on living animals or even humans.

1.3 Structure of the thesis

Based on the previously mentioned goals and non-goals of the thesis, the same is divided into four main chapters, i.e. Theory (see Chapter 2), Materials and methods (see Chapter 3), Results (see Chapter 4) and Discussion and outlook (see Chapter 5).

Chapter 2 covers the theory of the greater part of the thesis, simultaneous electrophysiological and fMRI recordings in Section 2.1. A minor part dealing with electrical microstimulation in nonhuman primates is outlined in Section 2.2. In Section 2.1 a general introduction and the motivation for simultaneous extracellular electrophysiological recordings and fMRI is given. Here, the additional value of the combined method compared to previously used single or combined technologies for mapping active brain states is outlined. Subsequently, the properties and origin of the fMRI and the extracellular electrophysiological signal in regard to its combination are outlined. The next part deals with the challenges which arise from the combination of both technologies in the MRI environment. Here, issues due to the gradient switching during fMRI signal acquisition, the subject's pulse and the scanner environment are outlined. Also, strategies for an optimal electrophysiological setup configuration in an MRI environment are given. Moreover, the initially

motivated application of EEG-fMRI in epilepsy is outlined. The limitations of this application are given. Active research work of extracellular microelectrode electrophyisological and fMRI recordings in the macaque brain are additionally shown. The theoretical part of electrical microstimulation of this thesis is kept short due to the fact that the development and characterization of the same was only a minor part. Here, a general introduction and motivation for the technology in an MRI environment is given. Furthermore, a concrete application in the study of face expression is given. This will be the main application of the microstimulation device developed within this thesis at a later time.

In Chapter 3 all materials and methods used within this thesis are described in detail. Initially, in Section 3.1 three commercial available systems for broadband signal recordings including their hardware and software are outlined. The exact setup instrumentation solution for recordings of single cells and LFPs generated with a signal generator outside an MRI environment are given for each system. The next Section 3.2 deals with the necessary modification of one of the previously characterized systems. For this system two possible solutions for setup instrumentation in an MRI environment are outlined. The first one is able to measure broadband signals generated with a function generator and the second one is used to do a general noise estimation of the instrumentation equipment with a simple resistor. Finally, materials and setup configuration for the testing of the microstimulation device are outlined in Section 3.3.

Following Chapter 3, the results of the conducted measurements for all setup configurations and systems are given in Chapter 4. Initially, in Section 4.1 the results of Section 3.1 are outlined. Measurement data is post-processed in Matlab. Filtering and separation in the high frequent spikes and the low frequent LFPs is done. Time signals are displayed. Also, the single sided amplitude spectra are calculated for both signals and each system. The signal-to-noise ratio (SNR) is estimated for the spike data. Root-mean square (RMS), maximum and minimum amplitudes of each data set are indicated. Section 4.2 deals with the results obtained from Section 3.2. Measurement data is divided into baseline for all measurements conducted in a natural environment, static magnetic field for all measurements executed in the static magnetic field of an MRI scanner and scan for the data obtained during an fMRI scan. Again, the single sided amplitude spectra are calculated and discussed for all measurements conducted and each setup configuration. Subsequently, RMS, maximum and minimum amplitude values of all measurements are calculated and outlined. Also, the time signals are shown and discussed. Finally, in Section 4.3 the results for Section 3.3 are outlined and discussed. The stimulus current time signals at various positions are outlined in combination of the trigger signal and the voltage of the positive and negative outputs as previously mentioned. The amplitude of the stimulus current is obtained for different positions within the setup for a tungsten wire and a microstimulation electrode.

Finally, Chapter 5 gives a discussion and an outlook of the project. In Section 5.1 all results from Chapter 3 are discussed. In Section 5.2 further steps of the project are indicated.

2 Theory

The following chapter describes the theoretical background of simultaneous electrophysiological and fMRI recordings in Section 2.1. Also an introduction and application of electrical microstimulation in nonhuman primates are given in Section 2.2.

2.1 Simultaneous electrophysiology and fMRI

In Subsection 2.1.1 a general introduction and the motivation for doing electrophysiological recordings during fMRI are outlined. Subsection 2.1.2 describes the characteristics and properties of both signals, i.e. the electrophysiological signal consisting of single cell and local field potentials (LFPs) and the fMRI data. Moreover, the challenges rising from the combination of both technologies are outlined in Subsection 2.1.3. The main focus lies on the characterization of the inevitable artefacts that occur in the electrophysiological data due to the use of the instrumentation equipment in an MRI environment. In Subsection 2.1.4 some general optimization steps for an optimal setup configuration in an MRI environment excluding parameter settings of electronic devices are given. Finally, applications and future perspectives are outlined in Subsection 2.1.5.

2.1.1 Introduction and motivation

In neurosciences, the ultimate goal is to fully understand how the human brain works. This requires not only a wide range of knowledge about the physiological time-varying properties and working principles of the individual elements such as neurons or a cluster of neurons, but also complete brain maps representing the structural architecture and an understanding of spatially distributed time-varying neural networks [30].

Since its introduction in the 1990s, functional magnetic imaging has developed to the most widely used imaging technique for mapping brain activity and the dynamics of functional neural networks at wide-ranging spatial and temporal scales nowadays. Its primarily the later approach which played a significant role in the Human Connectome Project. Within this project researchers just recently achieved to create an updated, sharp, multi-layered, large-scale, digitized brain map. Anatomical and functional brain data from over 100 samples have been used to display both old and new functions and structures and its connectivity (see Fig. 2.1). The method's main advantages lie in the non-invasive nature, widespread availability, reasonable costs and very good spatial resolution (about 2 mm to 3 mm). In short, the method maps brain activity through the indirect detection of neural activity linked to changes in local blood volume, flow and oxygen saturation. Such metabolic changes can be

caused through a predetermined stimulus or task or also through randomly occurring processes in the resting brain [12].

Providing an outstanding spatial resolution down to the cellular and even subcellular level, extracellular electrophysiological microelectrode recordings are the method of choice to measure the activity of individual neurons or a cluster of them and thus display significant temporal fluctuations. The technology records discharges of neurons in the extracellular space and subsequently provides information about physiological properties and also how the activity contributes to the functional neuronal network [17].

To sum up, both techniques provide very valuable, but complementary insights for a better understanding of the functioning of the brain. However, using them separately does not sufficiently answer neurologist's research issues any more. A high interest developed in not only acquiring the anatomical and functional brain maps related to behavior and cognition, but also to understand the exact underlying neural activity. Conjoined anatomical, functional and physiological investigations of neural networks at different organizational levels is highly aimed [28].

Although extensive effort has been put into the development of a method to answer the above described issue, none of them have been completely satisfying so far. The combination fMRI with EEG studies suffered from poor spatial resolution of the EEG signal, making an exact determination of brain activation patterns and its underlying neural activity impossible (see [25, 26, 35]). The use of optical imaging with fMRI has been done by various research groups (see [18]). However, the optical imaging method is also based on changes in blood oxygenation and thus cannot make a reliable decision on the fMRI signal connected to neural activity [28].

Simultaneous recording of electrophysiological signals and fMRI recordings now have the potential to overcome these problems and thus contribute immensely to a better understanding of the brain functioning. Unfortunately, there are undesired interactions between both technologies, resulting in extremely high demands in the experimental setup configuration inside the MRI, data integration, patient safety and artefact prevention and removal strategies [28].

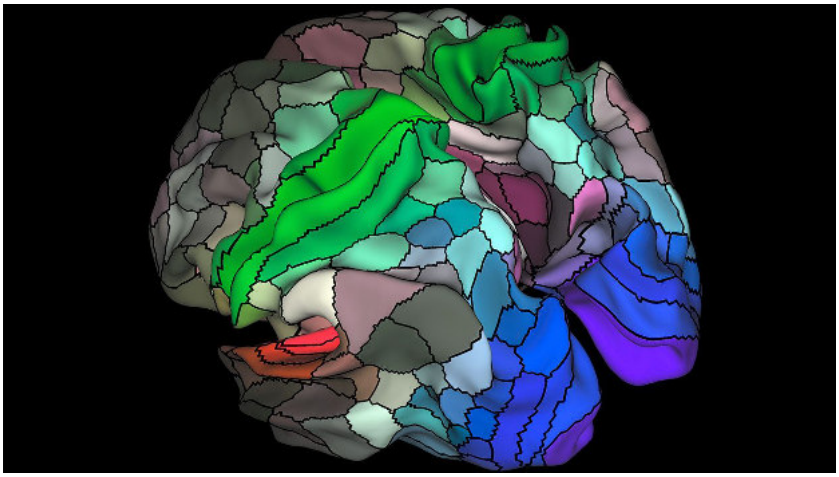

Figure 2.1: 2016 updated human structural and functional brain map from the Human Connectome Project. Areas connected to hearing (red), touch (green), vision (blue) and opposing cognitive systems (light and dark). Graphics from [58].

2.1.2 The signals

In the following, the basic features of both signals related to their combination are outlined. Firstly, the characteristics and properties of single cell and local field potentials (LFPs) are outlined, then the basics of the fMRI signal are described.

Single cell and local field potentials (LFPs)

In almost all invasive animal physiology studies, extracellular recordings are performed to measure neural activity in a spatially limited region and thus display time-varying potentials. LFPs are usually recorded in animals with low-impedance microelectrodes in the extracellular space around neurons. In general, a neuron is supposed to be inside an extracellular membrane. When the potential of two different parts of the neuron are different as signal processing is performed, there is current flow through the neuron that is matched to a return current through the extracellular space. LFPs represent the linear summation of sinks (active regions of the membrane) and sources (inactive regions of the membrane) of a population of neurons. Thus, when recording in a specific brain region, the measured signal consists of many different potentials of various amplitudes and sizes [17, 28, 34].

Normally, the action potentials (or spikes) representing the activity of a single cell and low frequency voltage variations are separated from each other by high and low pass filtering. Action potentials are obtained by using a high pass filter with a cut-off frequency of 300 Hz. The low frequency part of LFPs (in the following only denoted with LFP) are considered to be under 300 Hz. This frequency band separation can be explained by the fact that LFPs last much longer (from several milliseconds to 100 ms) and extend over a larger neural region than spikes (typically lasting only 0.4 ms to 0.5 ms). The voltage changes induced by LFPs are in the range of µV and much smaller than action potentials [17, 28, 34].

Functional magnetic resonance imaging (fMRI)

Unlike extracellular electrophysiological recordings, fMRI does not directly rely on neural activity. Instead it measures changes in oxygenation, local blood flow and volume. Increased neural activity, i.e. through artificial stimulation of a specific region with microelectrodes or through the performance of behavioral and cognitive tasks, causes a higher oxygen consumption in the designated area. Subsequently, the magnetic fields in the underlying neural tissue vary, as the hemoglobin has different magnetic properties depending on its oxygenation level. This magnetic field inhomogeneities can be detected in MRI scanners with high static magnetic fields. I.e. the quantity of brain activity due to stimulation or task-induced can be obtained through the extent and amount of blood flow over time. fMRI is normally performed using the blood oxygenation level-dependent (BOLD) contrast combined with an echo-planar imaging sequence (EPI). The EPI sequence is based on fast switching of the gradients with a maximum amplitude [28, 34].

2.1.3 Challenges

The concurrent use of a complete electrophysiological recording setup in an MRI environment entails several issues and challenges. A contamination of the measured electrophysiological signal due to the MRI scanner environment and the applied pulse sequences for image acquisition is expected and unfortunately not completely inevitable. As those artefacts can by magnitudes be higher than the desired signal, remarkable efforts to minimize them have to be put into during both signal acquisition and analysis.

The most problematic challenge comes from the basic physical principle of electromagnetic induction. In general, for the acquisition of electrophysiological data the creation of one or more conductive loops in a magnetic field is unpreventable, i.e. for single cell recordings a conductive loop between the microelectrode used for signal acquisition and the ground, which can be a second indifferent electrode (see [36]) or a simple ceramic screw (see [32] and [33]) is created. The Faraday's law of induction further states that every magnetic field interacting with an electric circuit, induces an electromotive force (emf) (see Equ. 2.1):

$$V_{induced} = A\frac{d_B}{dt} \tag{2.1}$$

whereby, $V_{induced}$ indicates the emf in the conductive loop, A is the loop area perpendicular to the static magnetic field B_0, and $\frac{d_B}{d_t}$ the magnetic flux change cutting the loop. Hence, any variation of the conductive loop area or magnetic field results in a change of the emf and thus induces an unwanted potential. This voltage adds to the real signal and causes distortion in the electrophysiological data [1].

Such variations in the conductive loop area can be caused by a number of different reasons. It can be due to the movement of the instrumentation equipment itself, scanner related vibrations, movements of the subject and also by an artefact associated with the subject's pulse. A variation of the magnetic field is caused by application of magnetic field gradient switching during the fMRI data acquisition. The highest rate of change of the magnetic field occurs by the application of the RF

pulses indicating the acquisition of a new volume. However, this frequency typically lies outside the desired frequency band at several MHz and thus can be simply removed by using an appropriate low pass filter. In the following the most important noise sources are outlined and characterized. All of them have been observed during simultaneous EEG and fMRI recordings. It is assumed that they are also valid for extracellular electrophysiological recordings [4, 40].

Gradient switching

The by far most dominant artefact is caused by the magnetic field gradient switching used for the spatial encoding during the fMRI data acquisition. As mentioned in Subsection 2.1.2 for the fMRI image acquisition usually fast switching gradients, i.e. EPI sequences, with maximum amplitudes are applied. According to Equ. 2.1 the switching gradients induce, depending on the maximum loop area, very high undesired voltages which can lead to saturation of the amplifier in the worst case. The gradient artefact is usually in the range of 10 mV to 100 mV for EEG recordings and thus most likely beyond the range of the electrophysiological signal [34].

An example of the gradient artefact waveform for a single slice is shown in Fig. 2.2. The artefact was acquired during the simultaneous acquisition of EEG and fMRI with an EPI pulse sequence. It is displayed for one EEG channel and one slice and repeats, every time a new slice is acquired. Note that the gradient artefact varies from the exact position of the electrode, the scanner environment and also the pulse sequence [41].

The artefact has a periodic matter with several spectral lines in the Fourier amplitude spectrum. In general, the power is concentrated in very narrow peaks. The most dominant frequency is obtained by the inverse of the slice repetition time, typically in the range of 10 Hz to 25 Hz. The second important frequency in the Fourier amplitude spectrum of the gradient artefact is the switching frequency of the readout gradient, usually between 500 Hz to 900 Hz. The volume acquisition frequency causes a frequency noise peak between 0.2 Hz to 2 Hz. Unfortunately, conventional low pass filtering is not applicable as the desired signal is typically broadband. Notch filters with very small stop bands could be used to filter only the gradient spike frequency. However, this procedure also attenuates the electrophysiological signal in the adjacent frequency range [1, 34, 56].

More complex artefact strategies have been reported previously. The very good characterization of the gradient switching artefact and reproducibility over several measurement sessions makes the removal of this artefact possible. In [2] a method is explained based on removing the imaging artefact from the continuous EEG by subtracting an averaged artefact waveform from the data set and then doing adaptive noise cancellation to eliminate the residual artefact. In [52] the reduction of this artefact is done by the application of an adaptive artefact restoration scheme. Moreover, restoration strategies for MRI gradient switching contaminated signals have been developed in [11].

Variations of the gradients switching artefact occur due to two sources. The first one is the slightly different timing of the electrophysiological signal sampling and the fMRI acquisition which can be immensely reduced by applying synchronization

of both technologies. The second one is due to movements of the equipment such as electrodes or wires and cables which cause variation of the conductive loop areas [56].

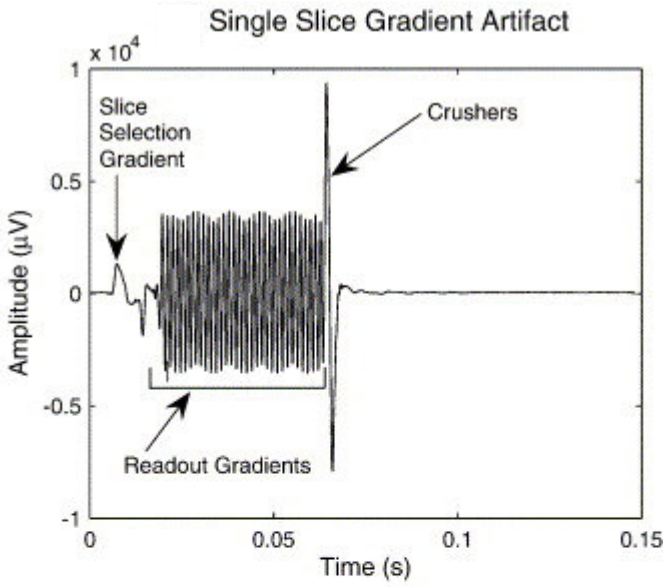

Figure 2.2: The waveform of the gradient artefact during the acquisition of a single slice in the EEG data. The x-axis shows the time in s and the y-axis the amplitude in µV. Some features related to the EPI sequence are labeled. The slice selection gradient initiates the start of the slice acquisition. The exact form of the readout gradient depends on the EPI sequence. Here, it is an oscillating wave. Crushers at the end of the readout gradients are used for correction before the next radio frequency (RF) pulse is applied. Graphics from [41].

Ballistocardiogram artefact

The ballistocardiogram or pulse artefact is related to the subject's cardiac cycle. Although the true origin of the ballistocardiogram interference is not known, it is most likely a combination of three main mechanisms:

1. The pulsatile blood flow in the subject's head, causes small, but impulsive expansion and contraction of the arteries between systole and diastole of the heart cycle. This can further result in the movement of the electrodes inside the static magnetic field and thus cause a slight variation of the conductive loop area.

2. Blood in general is considered as an electrically conducting fluid. Inside the magnetic field, the Hall effect leads to a charge carrier separation in blood vessels which produces a so-called Hall voltage. Pulsatile speed changes of the blood result in variations of the Hall voltage.

3. Small head and body movements during the cardiac cycle cause slight variation of the conductive loop area.

Correction of this artefact is a great challenge due to the fact that the pulse varies over time and various electrode positions. Moreover, it depends on the scanner environment and magnetic field strength B_0. As the general development of the MRI development aims to ultra-high fields, this effect becomes more and more enhanced [34, 40].

The ballistocardiogram artefact causes a peak at the heart rate frequency and its harmonics in the amplitude spectrum. Typically the amplitude is in the range of several µV in the time signal [1].

Again, well established and reported artefact subtraction methods are available and have been reported for the simultaneous use of EEG and fMRI. In [3] a method based on averaged artefact subtraction is as previously mentioned for the gradient artefact described and also applicable here. Further techniques depend on adaptive filtering methods, such as the independent component analysis (see [10]) and the optimal basis set (see [41]).

Scanner vibrations

Vibration related artefacts can be caused by all electrical devices in the scanner environment such as lights, infusion pumps, headphone systems and the camera at the back of the scanner bore [4].

However, the two most reported ones are the helium pump and ventilation system artefact. Nevertheless, results vary among literature.

The helium pump or compressor causes vibrations in the scanner's cyro cooling system which result in complex amplitude spectral profiles. Artefacts in the amplitude spectrum of the electrophysiological signal with broadband frequency power starting at 20 Hz to 30 Hz have been found in [42]. Here, the helium pump artefact was also dependent on different scanner models investigated. In [40] it was found that the helium pump effect depends highly on the mounting of the cold heads. Due to the fact that this artefact has an uncharacteristic, unstable and complex shape and thus is very unpredictable, many research group tend to switch off the helium pump during experiments. Turning off the helium pump during the fMRI data acquisition removes the artefact leaving only the line noise voltage and its harmonics. However, this is not advised and even prohibited in many clinical and research applications. As the helium pump is constructed for continuous use, switching off may cause malfunction of the pump or even a magnet quench in the worst case. Also, this procedure is accompanied by high costs which arise from the necessity of refilling the helium pump [40, 42]. A correction method for the helium pump artefact from EEG data has been reported by [59]. It is based on a method using carbon-wire loops as additional sensors.

The ventilation system artefact is most likely due to vibrations caused in the scanner which is directly transmitted to the electrophysiological instrumentation equipment and further cause small movements of the equipment in the scanner bore. Another possible source are electromagnetic fields transmitted from the ventilation engine which result in distortion. In contrast to the helium pump this artefact causes a specific peak and its higher harmonics in the amplitude spectrum. In [42] frequency peaks at around 37 Hz, 41 Hz and 50 Hz (for ventilation level 1, 2

and 3 respectively) were found. The artefact is in the range of several µV, typically lower than the gradient switching artefact and higher than the pulse related artefact. Slight variation across time and models were observed in the position of the frequency noise peaks and amplitudes. Post-hoc data restoration for vibration related systems is still an unsolved issue. Artefact removal strategies applied for the gradient switching or ballistocardiogram artefact are often not applicable due to the uncharacteristic temporal shape and variation across different scanner models and environments. Switching off the ventilation system eliminates the artefact. However, this results in a significant temperature rise and thus can pose a severe harm to the subject or the equipment [42].

2.1.4 Setup configuration optimization

An optimized electrophysiological setup inside the MRI environment minimizes artefacts severely and is crucial for a good data quality. In the following some general optimization steps related to the correct placement of the equipment in the MRI environment are outlined. The most important ones are the minimization of the loop areas and the use of non-ferromagnetic materials [46].

First, to minimize movement and thus reduce variations in the loop area, a proper fixation of all instrumentation related equipment and the subject's body is required. This can be realized by applying head fixation and securing the electrode leads and further equipment inside the scanner bore with tight bandage. Second, twisting and shielding of any wires and cables used in the magnetic field together, causes cancellation of emfs induced in adjacent cables or wires. This optimization step is shown schematically in Fig. 2.3. Unfortunately, this is not always practicable as some loop areas are inevitable [1, 40].

Also, the use of short leads and wires reduces variations in the loop area. Several studies have investigated the cable lengths and configuration on signal quality. While signal quality always increases by keeping the wires short for connection, the exact cable configuration for an optimized setup is highly dependent on the model of the scanner, magnetic field strength, and MRI environment. Thus, optimization strategies vary among literature and always have to be evaluated individually [4, 7].

Another important step is the electrical shielding of the pre-amplifier in the static magnetic field. This reduces electrical interference and signal distortion. However, it is ineffective against magnetic interference. Materials attenuating the magnetic interference however are often suspicious to change magnetic field homogeneity and thus avoided [30].

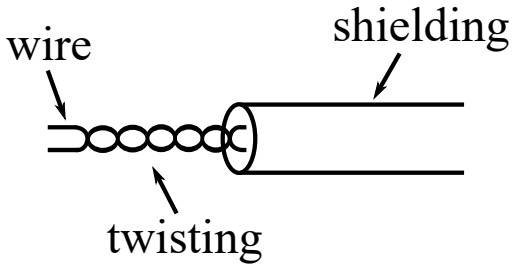

Figure 2.3: Setup optimization by twisting and shielding of wires.

2.1.5 Applications and future perspectives

Initially, the combination of electrophysiological recordings and fMRI was clinically motivated in the field of epilepsy. The study's main aim was the identification of the exact position of electrical sources related to epileptiform discharges and the thus caused hemodynamic change in the same region. The first EEG recording inside an MRI environment was performed in the 1990s (see [19]). Since then the method quickly developed from the research setting to being successfully applied in epilepsy centers for presurgical planning of patients with focal epilepsy. Although the study of epilepsy is still the most important clinical application, numerous other applications emerged. In cognitive neuroscience the technique made a tremendous contribution to better understanding the resting state. Here, the combined EEG-fMRI recordings are used to study spontaneous brain activity. Nowadays, applications of EEG-fMRI are widespread ranging from the study of physiological cognitive and behavioral functions to pathological events [38, 47].

Despite such achievements and valuable contributions of EEG-fMRI in clinics and cognitive studies, there are still some limitations of the technology. As mentioned in Subsection 2.1.2, the BOLD effect is caused by a variation of oxyhemoglobin in blood due to increased brain activity. Although the relationship between neuronal activity and the change in blood oxygenation can be studied on a large scale, the exact relationship between neuronal activity and the BOLD signal is not known or even controversially in EEG-fMRI across various studies. Recent studies now focus on the exact relationship between the BOLD signal and the correlated neural activity, i.e. LFPs and single cells. Here, the most important studies used simultaneous electrophysiological microelectrode recordings of LFPs and single spikes and fMRI in experimental animals. Studies in the cortex of macaques were performed in [30]. It has been found that the LFPs were a better predictor of BOLD variations than single- and multi-unit activities [30]. But not only the increase of the BOLD signal and its relation to neurovascular coupling are studied. A recent study conducted electrophysiological microelectrode recordings and fMRI in the macaque brain for the examination of the neuronal activity underlying negative BOLD responses. It could be successfully shown, that the negative BOLD response is associated with decreases in neuronal activity [49].

Adapting this technology of simultaneous electrophysiological recordings and fMRI for humans in the near future provides a huge potential. Not only that it would be possible to create a link to animal research studies, it would also widen the general understanding of the physiology and importance of the BOLD signal in various human brain networks and disease states [47]. In Fig. 2.4 a schematic setup of electrophysiological recordings in an MRI room is given. Some features related to microelectrode recordings in the brain are labeled.

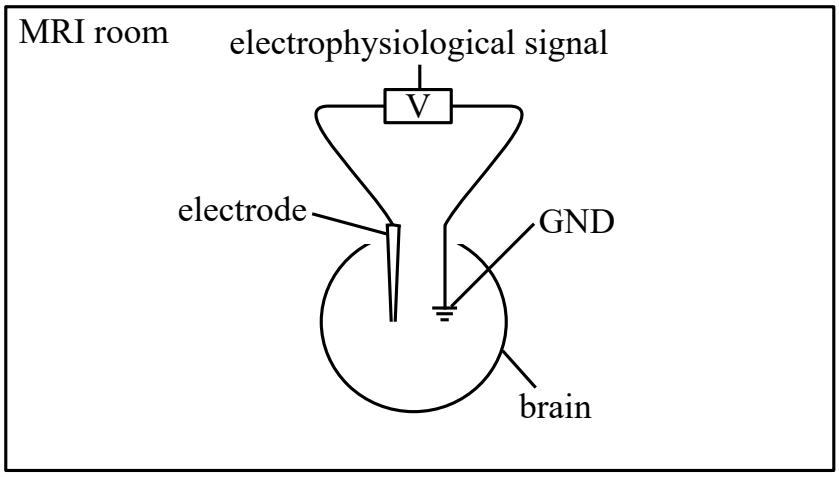

Figure 2.4: Schematic setup for electrophysiological recordings in an MRI room. The voltage difference between the electrode and the ground (abbreviated with GND) is acquired in the brain. The electrode is lowered in the brain to the region of interest. The ground can be a second indifferent electrode or tungsten wire.

2.2 Microstimulation

This chapter gives a general introduction of electrical microstimulation in Subsection 2.2.1. In Subsection 2.2.2 the specific application of the technique for the identification of the face processing system and its connectivity in the macaque brain is outlined.

2.2.1 Introduction and motivation

Electrical microstimulation in general is defined as the delivery of electrical currents with a specific shape to a predetermined brain region via a microstimulation electrode. Its main aim is to stimulate an area of interest and subsequently define functionally connected areas. During the last few years electrical microstimulation has gotten more and more attention in the study of the operational organization of the brain. So far, the method has contributed to valuable results in the discovery of functional maps connected to the visual and motor system. Also, it played a significant role in the discovery of specific brain regions responsible for sensory and cognitive functions. Recently, the technique also found applications in electrotherapy and neural prosthesis. However, there is very little knowledge about the actual signal propagation in brain tissue after the delivery of stimulation currents to a specific region, i.e. the cortical activity patterns generated by stimulation around the electrode and in distally and functionally linked regions is still unclear. To identify and establish the relationship of specific brain regions and its functionally connected areas, electrical microstimulation combined with simultaneous fMRI is the key technology and thus subject of active research [36, 44, 53].

2.2.2 Application

One of the most promising applications of electrical microstimulation is in the research field of facial expression. Uncommon and complex deficits in brain mechanisms responsible for facial expression have been identified as a result of localized brain trauma caused by injuries and diseases. As a result, alterations in perception, cognition, memory and movement execution might occur. The connectivity of so-called face patches, i.e. cortical areas consisting of an accumulation of neurons which are responsible for face processing, have been studied extensively in nonhuman primates. In general, faces are a category of complex objects which are supposed to selectively activate six patches in the ventral cortex of the macaque brain. Studies are concerned for instance with the question whether face processing is based on the sequence of subsequent processing stages or distributed representations. Depending on the precise research question that should be answered, a decision has to be made, including but not limited to the microstimulation device and accessory equipment such as the electrodes, the used microstimulation protocol and the experimental design [36, 37, 44].

3 Materials and methods

This chapter gives an overview of all materials and methods used within this thesis. Initially, in Section 3.1 the hardware and software of various commercial available systems for doing broadband electrophysiological recordings outside MRI environment are described. Then, in Section 3.2 two setups and its related materials for obtaining electrophysiological data inside MRI environment are explained. In Fig. 3.1 the systems characterized outside MRI environment and the two setups tested in MRI environment with the Tucker Davis system are shown. The same division is used in Chapter 4 and Chapter 5. Section 3.3 finally deals with the microstimulation setup developed and characterized within this thesis.

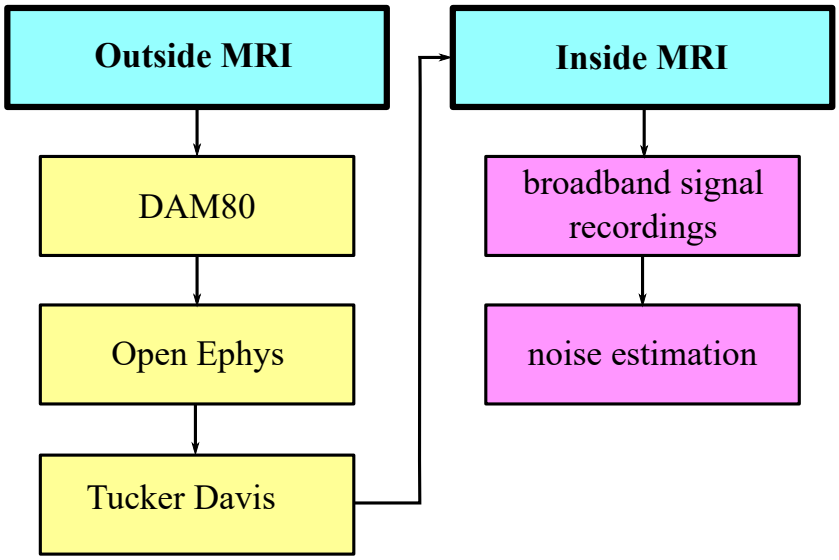

Figure 3.1: Approach for doing electrophysiological recordings inside MRI environment. Initially, the DAM80, Open Ephys and Tucker Davis systems are characterized outside MRI environment. Then the two setup configurations, broadband signal recordings and noise estimation, based on the Tucker Davis system are tested inside MRI environment.

3.1 Outside MRI environment

In a first step, different approaches for obtaining broadband electrophysiological signals outside MRI environment are considered. Subsequently, its results (see Section 4.1) are evaluated and discussed with regard to their suitability of use in MRI environment (see Subsection 5.1.1). Subsection 3.1.1 outlines a technique using the differential amplifier DAM80. Additionally, a measurement setup based on an open-

source project is described in Subsection 3.1.2. The final Subsection 3.1.3 deals with a high-end technology setup of the renowned company Tucker Davis in Florida, USA.

3.1.1 DAM80

The DAM80 is a differential amplifier offered by the company WPI (World Precision Instruments, Sarasota, USA) for extracellular signal amplification. It is battery powered to reduce line noise and allows the user to adjust general settings for recordings. The low pass filter can be set between 0.1 Hz, 1 Hz, 10 Hz and 300 Hz and the high pass filter between 0.1 kHz, 1 kHz, 3 kHz and 10 kHz. Moreover. the amplification factor can be chosen between 100, 1000 and 10 000 [60].

Hardware

A picture of the DAM80 is shown in Fig. 3.2 and a schematic overview of the overall measurement setup used to acquire broadband neural signals in Fig. 3.3. A Blackrock microsystems 128-channel neural signal simulator (Blackrock Microsystems LLC, Salt Lake City, USA) is used for the generation of neural signals. This simulator provides different waveforms of action potentials added to a LFP signal which itself is made of two superimposed sine waves at 3 Hz and 9 Hz. It is placed in a self-made Faraday cage of aluminum foil. One of its channels is connected to the input of the probe of the DAM80 differential amplifier (World Precision Instruments, Sarasota, USA). The reference of the device is connected via a mini banana plug-in to the reference of the probe. Additionally, the probe is grounded with a ground clip to the Faraday cage. To make sure that the amplifier does not produce any noise in the signal it is also grounded, although it is battery-operated and should thus not to be sensitive to grounding noise. The signal is transmitted via a BNC cable and further displayed on a Rohde & Schwarz HMO 1002 Series Oscilloscope (Rohde & Schwarz, Columbia, USA).

Figure 3.2: Graphic of the DAM80. The low pass filter can be set between 0.1 Hz, 1 Hz, 10 Hz and 300 Hz and the high pass filter between 0.1 kHz, 1 kHz, 3 kHz and 10 kHz. Moreover, the amplification factor can be chosen between 100, 1000 and 10 000. Further features are not used in this thesis [60].

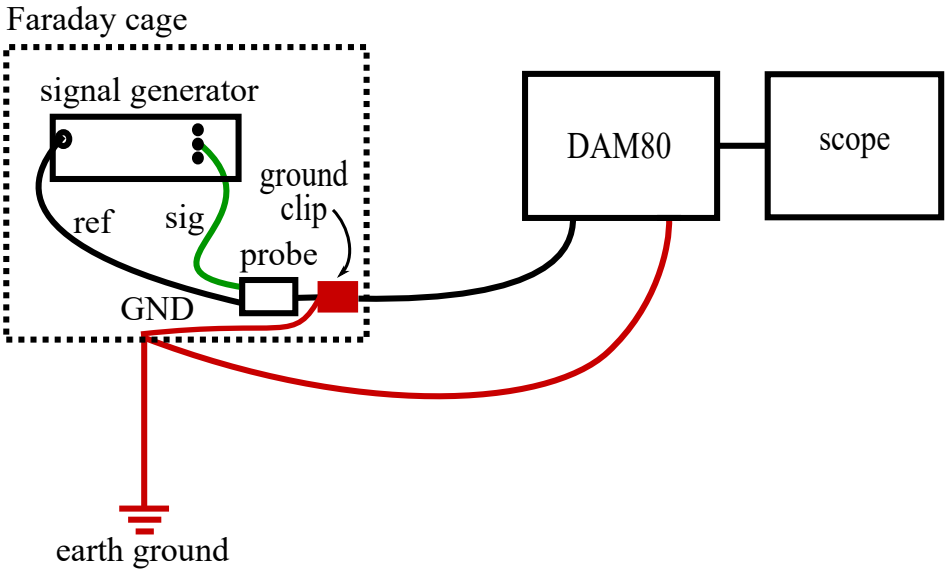

Figure 3.3: Measurement setup for acquisition of neural signals with the DAM80 differential amplifier. A 128-channel neural signal generator is used for the simulation of neural signals. Only 3 channels are shown in this schematic. It is connected with a self-made signal (abbreviated with sig) wire shown in green and a reference (abbreviated with ref) wire shown in black to the probe of the differential amplifier. The measurement side, i.e. the simulator and the probe is placed in a self-made Faraday cage, which itself is grounded to the earth-ground, shown in red. Also, the probe and the differential amplifier itself are connected to this ground (abbreviated with GND). The neural data is transferred from the simulator to an oscilloscope (abbreviated with scope) via a BNC cable for visualization.

3.1.2 Open Ephys

Open Ephys is an open-source project started by a group of neuroscientists for doing electrophysiological recordings and data analysis. The hardware is offered by the Open Ephys initiative and can be purchased very inexpensively. The software provides a huge number of tools for electrophysiological research. All of them are open-source, thoroughly documented and field-tested. The greatest advantages provided by Open Ephys are the flexibility to modify features to the user's needs, the ability to run experiments at low cost, scientific and educational benefits of the tools' transparency, and the reduced redundancy resulting from shared development efforts [51].

Hardware

Again, the Blackrock microsystems 128-channel neural signal simulator is used for the generation of LFPs and action potentials. The acquisition is done with the Open Ephys system (Open Ephys, J. Siegle and J. Voigts, USA). A schematic overview of the measurement setup is given in Fig. 3.5.

The key element of the overall setup is the Open Ephys acquisition board (shown in Fig. 3.4a). It is connected to a 5 V/ 6 W DC power supply via the power jack on the Xilinix Spartan 6 FPGA (Xilinx Inc., San Jose, USA) module on the backside. Digital data is transmitted from the FPGA unit via an USB cable (Opal Kelly, Portland, USA) to a standard PC with a sampling rate of 30 kHz. Digital neural data is transferred via a SPI cable (Intan Technologies, Los Angeles, USA) from the probe to the acquisition board. A RHD2132 Intan amplifier (Intan Technologies, Los Angeles, USA) is used as a headstage in this study (see Fig. 3.4b). It filters and amplifies the input signal. An analog-to-digital converter inside the chip digitizes the signal with a 16-bit resolution. A 36 pin Omnetics wire adapter (Omnetics connector corporation, Minneapolis, USA) is connected to the headstage. This wire adapter is modified in order to be able to record from only one channel. An alligator clip is soldered to one signal channel for connection to the neural simulator. All other signal channels remain unused and are cut short to reduce noise, stripped with a simple match, twisted, soldered together and then connected to the Faraday cage. The two reference wires are also twisted together and then soldered to a mini banana plug-in for connection to the simulator. For the acquisition of the neural data three different configurations of the setup are tested and its results compared in Subsection 4.1.2:

1. floating Faraday cage: Connection of reference channels to the reference pin of the neural signal simulator. For this purpose the two reference channel wires are twisted and soldered together.

2. grounded Faraday cage: Connection of the two reference channels to the reference pin of the neural signal simulator and of the Faraday cage to the common earth ground.

3. grounded Faraday cage and ref connected to GND: Connection of the reference of the simulator to the ground of the Faraday cage and of the Faraday cage to the common earth ground.

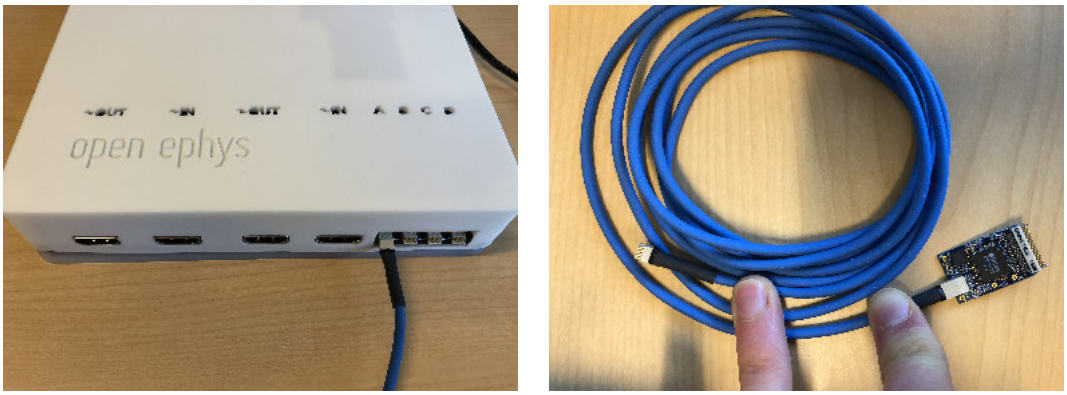

(a) (b)

Figure 3.4: (a) Picture of the Open Ephys acquisition board. On the left side there are contacts for I/O devices. The right side shows the inputs for the digitized data from the probe. (b) Picture of the headstage and SPI cable.

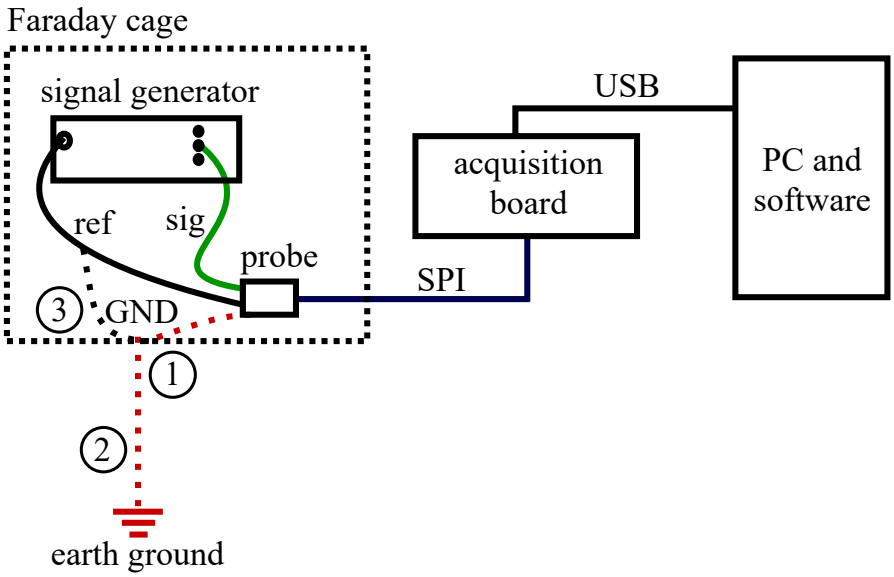

Figure 3.5: Schematic overview of the setup for the acquisition of neural signals with the Open Ephys system. LFP and spike data from a 128-channel neural signal generator are transferred via a signal (abbreviated with sig) cable connected with an alligator clip to a pin of the neural simulator and soldered to the wire of one channel of the wire adapter. The reference (abbreviated with ref) wire is plugged to the reference of the simulator and handled according to the setup configuration. Also the variation in the common ground (abbreviated with GND) and earth ground result from the different setup configurations tested. Note that only three of the 128 channels are displayed in this visualization. The noise sensitive side of the measurement setup is put in a Faraday cage for shielding purposes. The headstage as part of the probe digitizes, amplifies and filters the signal. It is connected via a SPI cable to the Open Ephys acquisition board which itself transfers the data via USB connection to a standard PC for further analysis in the Open Ephys software.

Software

An initial data display and first analysis is done with the Open Ephys GUI (Open Ephys, J. Siegle and J. Voigts, USA). The post-processing is afterwards done in Matlab R2017 (MathWorks, Natick, USA).

The Open Ephys GUI is based on C++ and is used to acquire, filter and visualize neural data. For this purpose, a signal chain is created with the provided modules. The signal chain created for this experiment is displayed in Fig. 3.6. The Rhythm FPGA is used as source. This module receives data from the FPGA running Intan's Rhythm firmware. Here, the sampling frequency is determined with 30 kHz which is above the minimum sampling frequency for extracellular neural signals according to [39]. The continuous LFP signal is streamed with the LFP viewer as output. It is filtered between 3 Hz and 300 Hz with a bandpass filter. Furthermore, the spike viewer which displays spikes in real-time is used as output. Before using the spike viewer a bandpass filter with a low cut of 300 Hz and a high cut of 5 kHz is

applied. The settings of the bandpass filter are chosen based on the suggestions of [48]. Moreover, a spike detector is necessary after the filter and before the spike viewer. Within this module the recording type of electrodes for the spike detection is chosen. In this study one single electrode is used. Also, the threshold is set to 50 µV in the spike detector. A splitter is used to switch between the LFP and spike viewer. The LFP viewer shows the low pass filtered signal. The software allows the user to adjust the input range in µV and the time base in s in the LFP viewer window. The spike viewer displays the detected spikes above a certain threshold which can be set manually by the user [51].

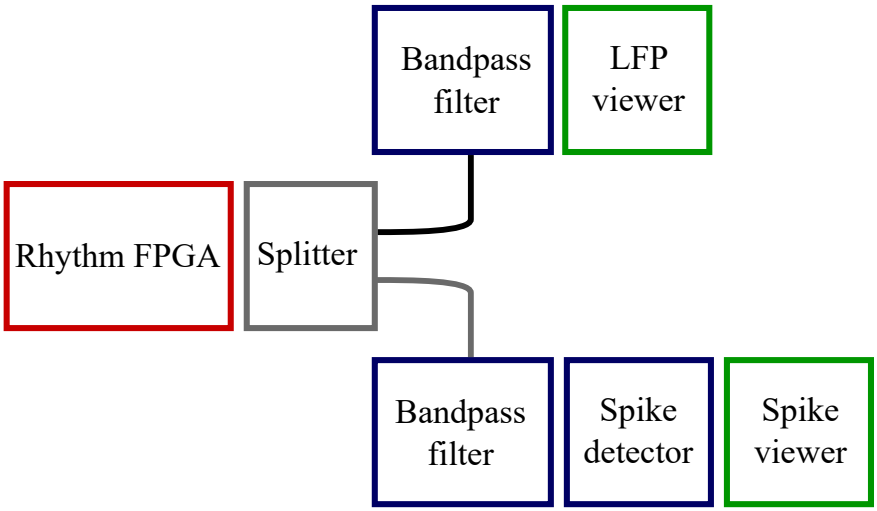

Figure 3.6: Signal chain for data acquisition. The Rhythm FPGA with a sampling frequency of 30 kHz is used as sink. The bandpass filtered LFP signal is displayed with the LFP viewer. The spike viewer is used to show the detected spikes in real-time. A bandpass filter is applied between 300 Hz and 5 kHz for this purpose. Also, a spike detector is used to set the recording type to single electrodes and the threshold to 50 µV. A splitter is used to switch between the LFP and spike viewer.

3.1.3 Tucker Davis

The company Tucker Davis Technologies also provides high-end workstations for doing electrophysiological recordings of LFPs and single cell spiking activities. In the following the hardware and software for the developed measurement setup are described in detail.

Hardware

The hardware setup is based on equipment from the company Tucker Davis (Tucker Davis Technologies, Alachua, USA). Graphics of the setup are shown in Fig. 3.7 and Fig. 3.8. A schematic overview of the acquisition system for neural signal recordings outside MRI environment is given in Fig. 3.9.

LFPs and spikes are again generated with the Blackrock microsystems 128-channel neural signal generator. For connection of the simulator to the 16 channel LP16CH-

ZNF headstage used within this study, a reusable "headstage-to-electrode adapter" is designed. The adapter is made fully MRI compatible and also attachable to electrodes for later animal studies. For this purpose, an OM16-M-F-Jumper_MRI jumper cable (Neuronexus, Ann Arbor, USA) is modified in the following way: First, the cable is cut in the middle. Then a female miniature pin connector, catalog # 520100, (A-M Systems, Sequim, USA) is grimped and soldered to CH1 of the headstage. Another female connector is grimped and soldered to the reference channel. All other channels remain unused. They are cut as short as possible, soldered together, connected to ground and wrapped in isolation bandage. The headstage inputs are by default single-ended with reference and ground tied together. For further connection of the adapter to the simulator two wires with each having a male miniature pin connector, catalog # 520200, (A-M Systems, Sequim, USA) on one end are made. The wire for signal acquisition is soldered to an alligator clip and connected to a channel of the simulator. The wire for referencing is stripped on the other end and connected to the reference of the simulator (see Fig. 3.8a for visualization). The simulator is grounded to the Faraday cage, which is connected to the earth ground.

In this study the 16 channel LP16CH-ZNF headstage which is recommended for extracellular electrophysiological studies by the vendor is used. The headstage consists of only non-ferrous components, making it suitable to use it in an MRI environment and even during fMRI imaging in Section 3.2. The headstage is an impedance converter with an unity gain and a high input impedance of $10^{14}\,\Omega$. It is directly connected to Bank A on the back-panel of the 32 channel count pre-amplifier PZ5. The PZ5 is battery powered and optically isolated and thus almost insensitive against any line noise. The pre-amplifier's very large input range ($\pm 500\,\mathrm{mV}$) avoids almost every signal saturation from movement or other artefacts (see Section 2.1.3). It uses oversampling and signal averaging and thus reduces the background noise and increases the SNR. The sampling rate of the amplifier is set to the system's sampling rate (around 25 kHz) and the onboard downsampling filter is set to 45 % of the sampling rate. Further settings of the PZ5 are configured in this study to single unit recording, the local reference mode, AC coupling and no external ground [55].

The signals are digitized and amplified within this device and then transmitted to the RZ2 amplifier via a 5 m fiber optic connection for processing. In parallel, configuration information is sent from the RZ amplifier to the PZ5 neurodigitizer across this fiber optic connection. The transferring of the maximum possible 16 channels is done simultaneously with a sampling rate of around 25 kHz. However, in this study only one channel is used. The RZ2 base station processor features two digital signal processor (DSP) cards for real-time signal processing and simultaneous acquisition. Furthermore, this processor has 16 channels of digital I/O. One of them is used in Section 3.2 to monitor the trigger signal of the gradient switching. The processor has an onboard optical connection interface to the PO5 Optical PCI Express Card for hardware control implemented in a Dell Precision 5820 Tower PC server (Dell Technologies, Austin, USA). The RZ2 is further connected to an AC power supply (110 V). The touchscreen of the RZ2 shows information about each DSP, the optical PC interface, the connected PZ5 pre-amplifier and system I/O. The analysis of the acquired signal and the setting of the PZ5 configuration parameters

are done in the TDT software Synapse (Version 86) [55].

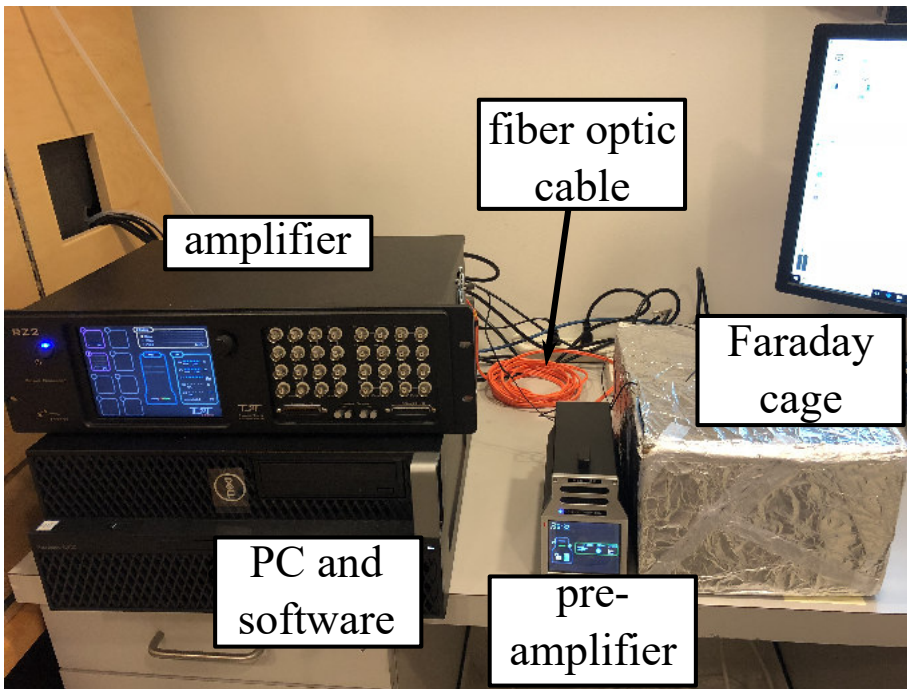

Figure 3.7: Picture of the setup. Inside the Faraday cage are the noise sensitive parts of the setup, i.e. the signal generator and the probe. The probe is connected to the pre-amplifier which transfers the signal via a fiber optic cable to the amplifier. Hardware and software control of the amplifier is done with the software Synapse installed on a PC.

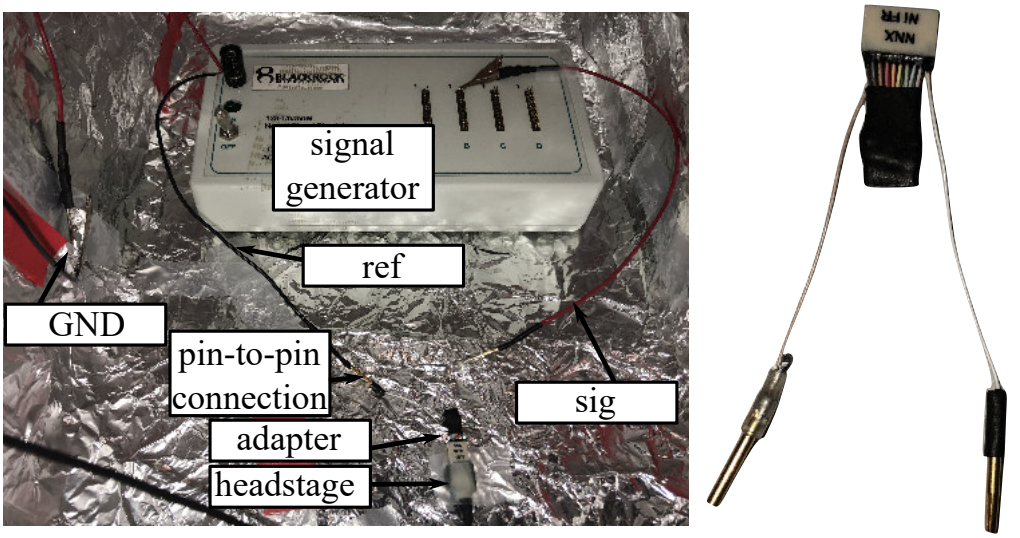

(a) (b)

Figure 3.8: Graphics of the measurement setup. (a) Picture of the noise sensitive part inside the Faraday cage. The "headstage-to-electrode adapter" is connected to the headstage which are together indicated as probe in Fig. 3.9. A pin-to-pin connection is used to connect the signal (abbreviated with sig) and reference (abbreviated with ref) wires to the adapter. The signal wire is connected to a signal channel of the simulator with an alligator clip. The stripped part of the reference wire is connected to the simulator. The simulator is grounded (abbreviated with GND). (b) Picture of the designed "headstage-to-electrode adapter". A jumper cable is cut in the middle. Two female pins are soldered and grimped to CH1 and the reference channel. A transparent shrinkage voltage is used for the signal channel and a black one for the reference channel. All other channel wires are cut as short as possible to reduce noise, soldered together, connected to ground and wrapped in black isolation bandage.

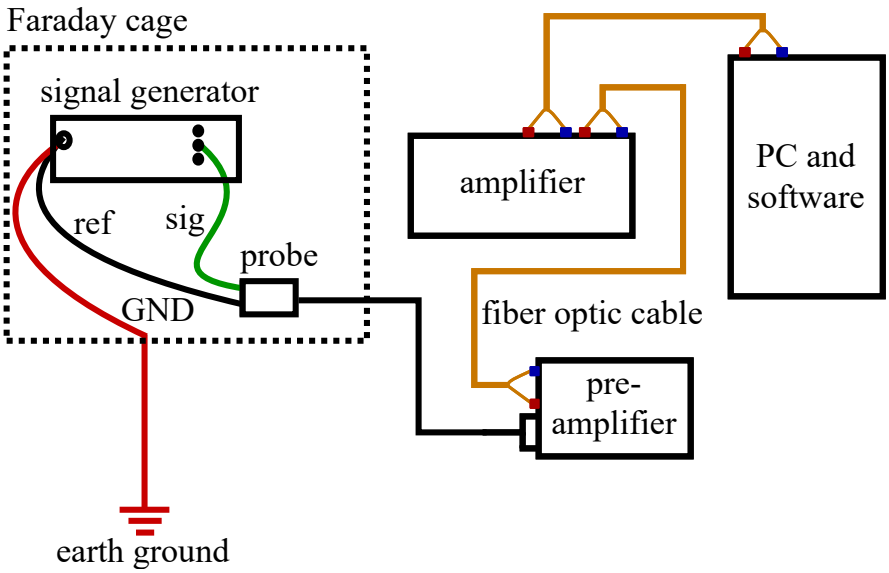

Figure 3.9: Electrophysiological signal acquisition system of the company Tucker Davis. A neural signal generator is used as signal source. The probe in this study consists of a "headstage-to-electrode adapter" and the 16 channel count headstage itself. The signal (abbreviated with sig) and reference (abbreviated with ref) channels of the probe are connected to the simulator via self-made wires. The simulator is grounded to the Faraday cage (abbreviated with GND) which itself is connect to the earth-ground (shown in red). Analog signals are transferred from the probe to the pre-amplifier. Each fiber optic cable has a connector for the input (blue) and one for the output (red). The pre-amplifier digitizes and amplifies signals and sends them via a fiber optic cable (shown in orange) to the amplifier which sends the digitized signals again via a fiber optic cable to the Optibit Express card implemented in a PC. The control of the amplifier is done in the software Synapse.

Software

The software Synapse is used to design the experiment, manage the settings and collect data from the hardware. In the design phase of the experiment Synapse automatically detects the connected hardware in the editor rig. In this study a premade experiment template is used for displaying and analyzing the LFP and spike data. In the manage phase Synapse requires information about the user, the experiment and the subject. Once these settings are applied, the settings of the so called Gizmos can be changed in the processing tree. A schematic overview of the processing tree is given in Fig. 3.10. The settings of all instrumentation devices displayed can be changed by double-clicking on them. For the RZ2 a sampling rate of 25 kHz is chosen. For the PZ5 the number of channels is set to 16. Also, the settings of the Gizmos for data display, analysis and storage are changed. For the spike sorting Gizmo based on the principal component analysis (PCA), the auto thresholding mode is chosen (indicated with *Neu1* in Fig. 3.10). The range of the spikes is determined, as in the previous study, to be between 300 Hz and 5 kHz. The

storage of the spike data waves is done with a maximum sampling rate of 24 414 Hz (system's rate) in the TDT data tank format. For the filtering of the LFP data a high pass with 3 Hz, a low pass with 300 Hz and a Notch with 60 Hz are applied (indicated with *Lfp1* in Fig. 3.10). As soon as the experiment is fully configured and saved, the recording is done. The run time window includes tabs with the main data plot and run time controls for each Gizmo. The data is saved to disk in real-time. The basic window consists of a plot for each type of data being recorded and saved (filtered multi-channel floating LFP signal, neural spike signal and snippet data including timestamp, short waveform, and sort code). The threshold detection is based on a calculation of the deviation of the waveform from its RMS. The software keeps track of run time settings and modification of parameters which can be accessed in the digital Lab Notebook [54].

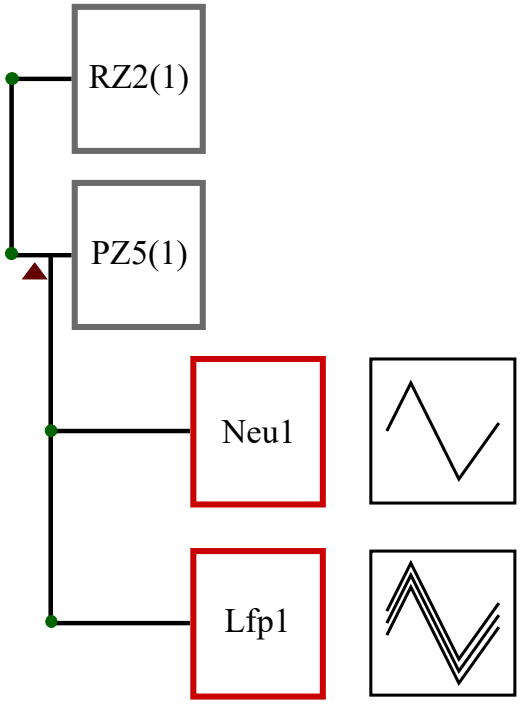

Figure 3.10: Processing tree for the premade experiment template *LFP_PCASort*. The software automatically detects the processor *RZ2(1)* and the preamplifier *PZ5(1)* and lists them in the processing tree for setting modifications. The neural signal (neural spike signal and snippet data including timestamp, short waveform, and sort code) are displayed with the Gizmo *Neu1*. The Gizmo *Lfp1* shows the filtered multi-channel floating LFP signal in the runtime window.

3.2 Inside MRI environment

In this chapter the materials and setup modifications used to characterize the Tucker Davis system in MRI environment are described. In Subsection 3.2.1 broadband signal recordings are done with a function generator. In the second approach (see Subsection 3.2.2) a 930 kΩ resistor is put in between the signal and reference channels

to simulate resistance in the brain and make a general noise estimation.

3.2.1 Broadband signal recordings

In a first step a solution for transferring the signal with as low noise as possible from the control room inside the MRI environment has to be considered, as there are no MRI compatible signal generators available. In order to transmit the signal from the signal generator placed in the control room via wave guides in the patch panel inside the MRI room, two extension wires with a length of around 5 m each are installed with a pin-to-pin connection between the adapter and the simulator. Initially, the same Blackrock simulator as in Subsection 3.1 is used as signal generator. However, a test measurement in the MRI control room shows that the noise level increases up to ±300 µV and thus exceeds the useful signal range. As the spikes characterized in Section 3.1 only show amplitudes up to ±200 µV, the use of this neural simulator is not reasonable here.

The next approach for testing the setup is based on broadband recordings from a 7 MHz sweep function generator, model 4007 DDS (B&K Precision, Yorba Linda, USA). This function generator is able to produce output amplitude voltages between 600 mV to 20 000 mV peak-to-peak value into an open circuit. As mentioned in Subsection 3.1.3 the input range of the Tucker Davis pre-amplifier is only ±500 mV. In order to reduce the signal to an amplitude low enough to not damage the pre-amplifier, a voltage divider is designed and placed after the output of the function generator to lower its output. For this purpose, two resistors are soldered together. The connection to the function generator is made with alligator clips. Pins are used to connect to the extension wires on the other side. The voltage divider is shown in Fig. 3.11b. Resistor R_1 has a value of 12 Ω and for R_2 a value of 12 kΩ is chosen, resulting in a division factor of around 1000 of the input voltage. The input voltage V_{in} is set to around 600 mV. According to the voltage divider equation: $V_{out} = V_{in} \cdot \frac{R_1}{R_1+R_2} = 0.6 \cdot \frac{12}{12+12000} \approx 599.40\,\mu V$ an output voltage of around 600 µV is achieved in this case which is strong enough to overcome the noise level and at the same time close enough to real spike voltage amplitudes. All other materials and settings remained the same as in Subsection 3.1.3.

Baseline

A picture of the measurement setup for acquiring broadband signals in the MRI control room as baseline is shown in Fig. 3.11a. The signal from the function generator is applied to the voltage divider with two alligator clips. The by the factor 1000 decreased output voltage signal is transferred via a pin-to-pin connection from the voltage divider and extension signal and reference wires to the adapter and the headstage. Additionally, the output voltage measured after the voltage divider and the voltage delivered to the headstage after the cables are monitored with an oscilloscope. Further setup configurations after the probe are the same as seen in Fig. 3.7 and Fig. 3.9. Sine waves with five different fundamental frequencies (10 Hz, 100 Hz, 500 Hz, 1000 Hz and 2000 Hz) and an amplitude of around 600 µV are generated and recorded.

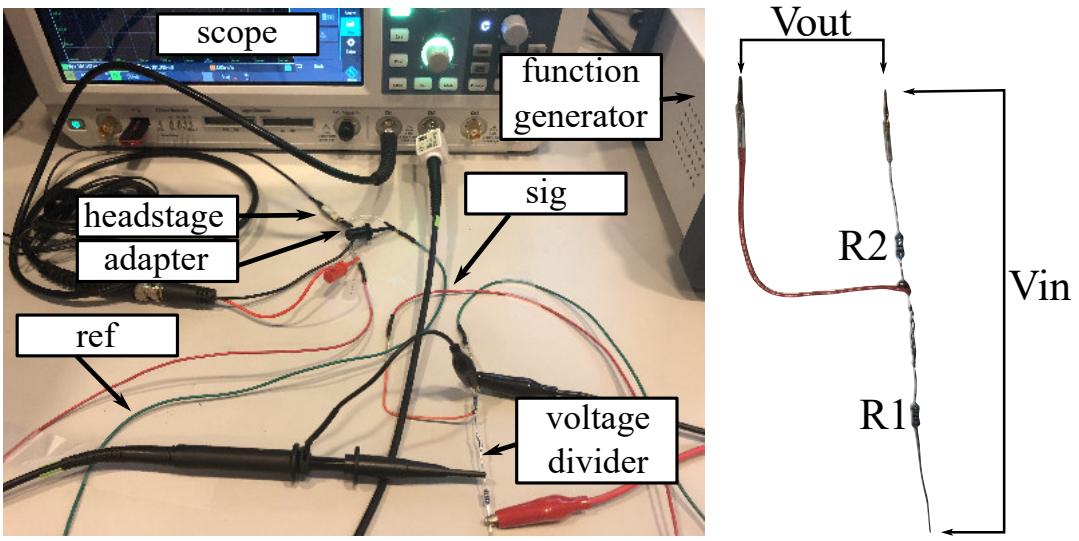

(a) (b)

Figure 3.11: a) Function generator measurement setup. Voltage is delivered from the function generator to the voltage divider and then transferred via the signal (abbreviated with sig) and reference (abbreviated with ref) extension wires to the adapter and headstage. Connections are made with pins. The divided voltage is monitored before and after the wires with an oscilloscope (abbreviated with scope). b) Picture of the voltage divider. The input voltage V_{in} of the function generator is divided by the factor 1000 with $R_2 = 12\,\mathrm{k}\Omega$ and $R_1 = 12\,\Omega$. The output voltage V_{out} is delivered via extension wires to the adapter and headstage.

Static magnetic field

In a next step recordings are conducted in the MRI environment and signal changes due to the static magnetic field B_o are observed. For this purpose, the headstage and adapter are placed in the middle of the 3.0 T Siemens Prisma Fit MRI scanner bore (Siemens Healthcare GmbH, Erlangen, Germany). Connection to the function generator is done as described above with two extension wires which are put through the wave guides of the patch panel. Output signals of the function generator are decreased with a voltage divider and monitored with an oscilloscope. The pre-amplifier also has to be placed inside the magnetic field of the scanner due to the inconvenient dimensions of the MRI room. However, it is placed as far as possible away from the scanner bore as the magnetic field B_o is the strongest in the middle of the bore and decreases with distance. Amplified and digitized signals from the pre-amplifier are transmitted via a fiber optic cable through a wave guide of the patch panel to the amplifier and finally to the PC for processing and display in the software Synapse. The schematic setup of the recordings done in the magnetic field is shown in Fig. 3.12.

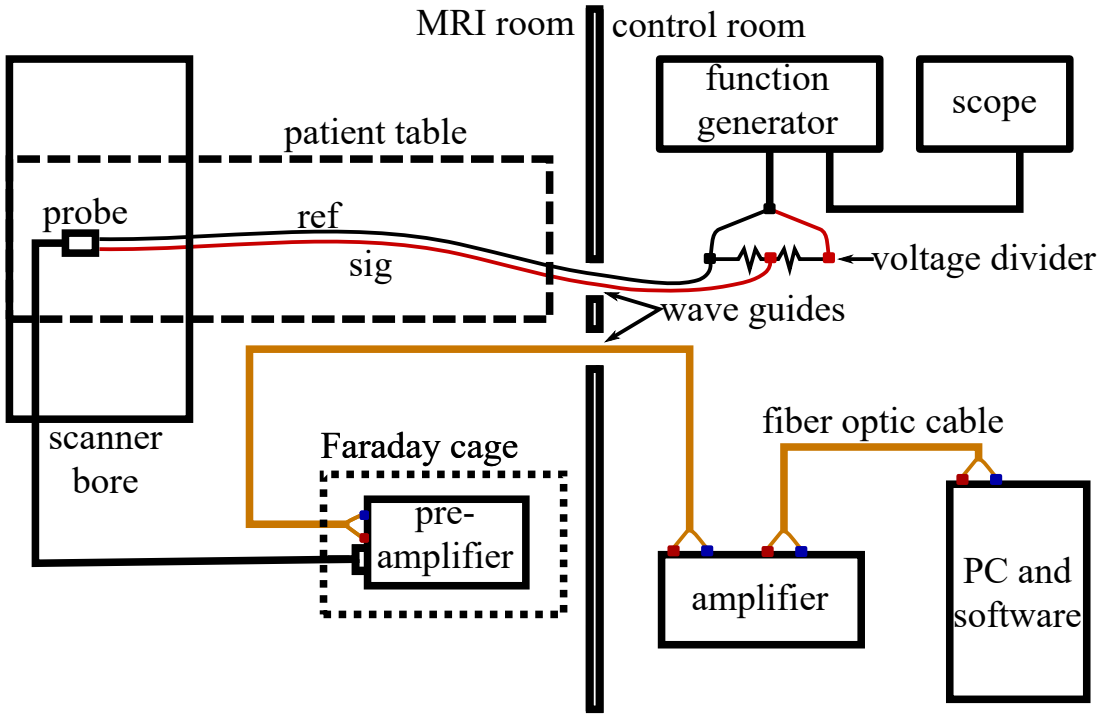

Figure 3.12: Setup for doing broadband signal recordings in the MRI room with a function generator. 600 mV sine waves are generated with a function generator placed in the control room. A voltage divider is used to decrease the input voltage to the system by the factor 1000. Signals after the voltage divider are monitored with an oscilloscope (abbreviated with scope) and transferred with two wires to the probe over wave guides in the patch panel. The signal wire (abbreviated with sig) is shown in red. The wire connected to the reference (abbreviated with ref) of the probe is shown in black. The probe is placed in the middle of the scanner bore and mounted on the patient table. Analog signals from the probe are amplified and digitized in the pre-amplifier which is placed in a Faraday cage inside the scanner room. Connection of the pre-amplifier to the amplifier is done with a fiber optic cable. Signals from the amplifier are transferred in real time to the PC. The Synapse software is used for analysis.

Scan

For the recordings inside the scanner the same setup configurations as before are used. A phantom made out of a plastic dummy brain filled with distilled water is positioned under the probe. An 8 channel loop transmit and receive coil is placed over the dummy brain. An EPI sequence is applied for simulating an fMRI scan. The field of view (FOV), slice thickness, gradient intensity and time profile are according to standard manufacturer's specifications.

3.2.2 Noise estimation

The setup configuration and settings are very similar to Subsection 3.2.1. The only difference is that here a 930 kΩ resistor is used as signal source instead of the function generator for a general noise estimation of the overall instrumentation equipment. The resistor is simulating the resistance in the brain. For connection of the resistor to the adapter pins are used. A schematic overview is shown in Fig. 3.13.

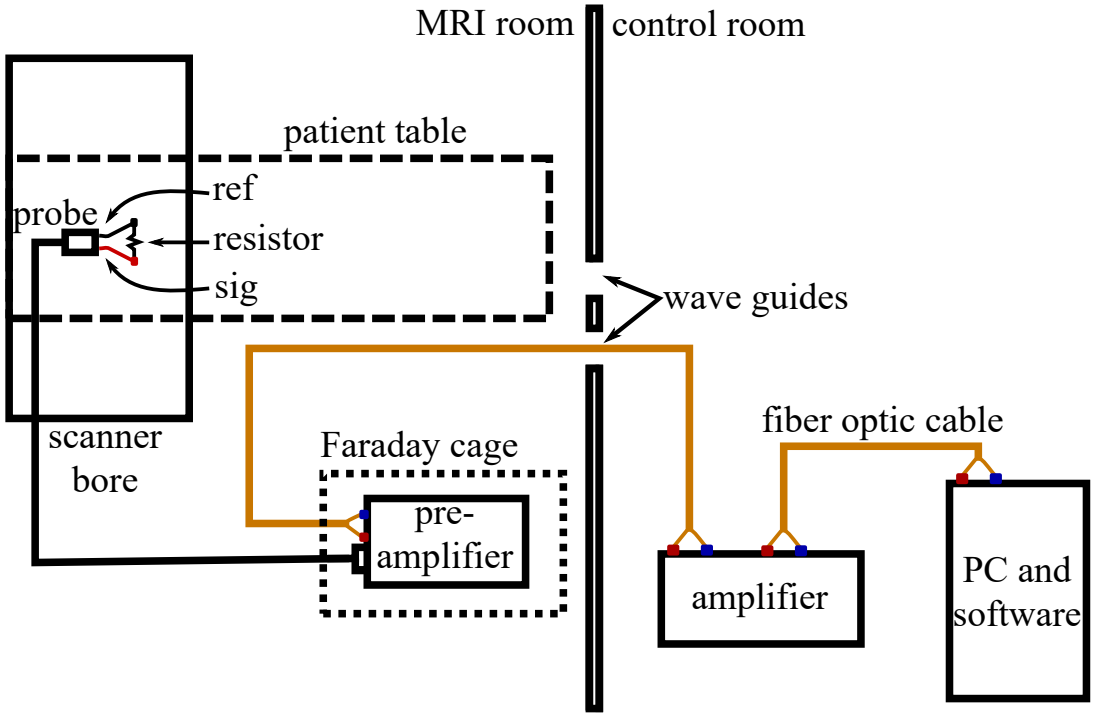

Figure 3.13: Schematic overview of the setup configuration used for the acquisition of broadband signals with a resistor simulating the resistance of the brain as signal source. All other configurations and settings remained the same as in Fig. 3.12.

3.3 Microstimulation

An A-M systems model 4100 isolated high power programmable stimulator (A-M Systems, Sequim, USA) is used for the generation of 200 ms pulse trains composed of 60 biphasic current pulses with an amplitude of 600 µV applied at a pulse frequency of 300 Hz. A schematic overview of the ideal current pulses is shown in Fig. 3.16. The design of the current trains is done according to [36].

The schematic overview of the MRI compatible test microstimulation setup is displayed in Fig. 3.15 and respectively. The stimulus current is delivered from the positive output of the stimulator and subsequently transferred over a 10 kΩ test resistor to cause a voltage difference. In order to put the resistor in the measurement chain, two banana plugs (Newark, Chicago, USA) are glued together and the resistor is soldered in between them (see Fig. 3.14a). The voltage difference equivalent to the stimulus current is acquired with a 25 MHz high-voltage Keysight Technologies,

model N2791, differential oscilloscope probe (Keysight Technologies, Santa Rosa, USA). The voltage is acquired at the positive and negative output of the stimulator with two standard Rohde & Schwarz RT-ZP03 passive probes (Rohde & Schwarz, Columbia, USA), displayed in Fig. 3.14b. For the acquisition of the positive output signal one probe is before the test resistor and grounded to the metal handle of the stimulator. For the acquisition of the negative voltage, a test clip to banana plug (Newark, Chicago, USA) is used in combination with a standard passive probe. The grounding is done in the same way as for the positive output. All signals are monitored with a Rohde&Schwarz RTB 2004 oscilloscope (Rohde&Schwarz, Columbia, USA).

A 2 m BNC to banana test lead (Newark, Chicago, USA) is installed for current transfer. To make sure that the distance between the brain and the stimulator is long enough for being able to do microstimulations inside the scanner, but having the stimulator outside in the control room at the same time, a 15 ft BNC cable (Newark, Chicago, USA) is further used to make a longer connection. To connect to the 2 m BNC to banana test lead, a female-to-female adapter (Newark, Chicago, USA) is necessary. Subsequently, for separation of the positive from the negative signal in the measurement chain a female to dual banana plug adapter is used (Newark, Chicago, USA). To reduce noise in the MRI environment, see Chapter 2.1.3, the signal is transmitted over a twisted dual banana cable (Newark, Chicago, USA). A test clip to banana plug is used to connect to a 10 kΩ test resistor on the positive output to cause a voltage difference. The test resistor of the positive output is initially connected to a 400 kΩ tungsten wire, catalog # 717200 (AM-System Sequim, USA) and then to a 50 kΩ to 100 kΩ tungsten microelectrode, catalog # UEWLEGSEAN1E (FHC, Bowdoin, USA). A dummy brain made out of a hollow polypropylene ball (McMaster - carr, Robbinsville, USA) and filled with a 2 % Agarose mixture is used for mimicking brain conditions. A return tungsten wire connected to the negative output is placed in the dummy brain for reference. Again a 10 kΩ test resistor is switched between the negative output and the tungsten wire. For connection of the electrode / tungsten wires to the resistor pins are crimped to each end again. In Fig. 3.14c the dummy brain and the tungsten wire / electrode and the return tungsten wire, each connected to a resistor, are shown.

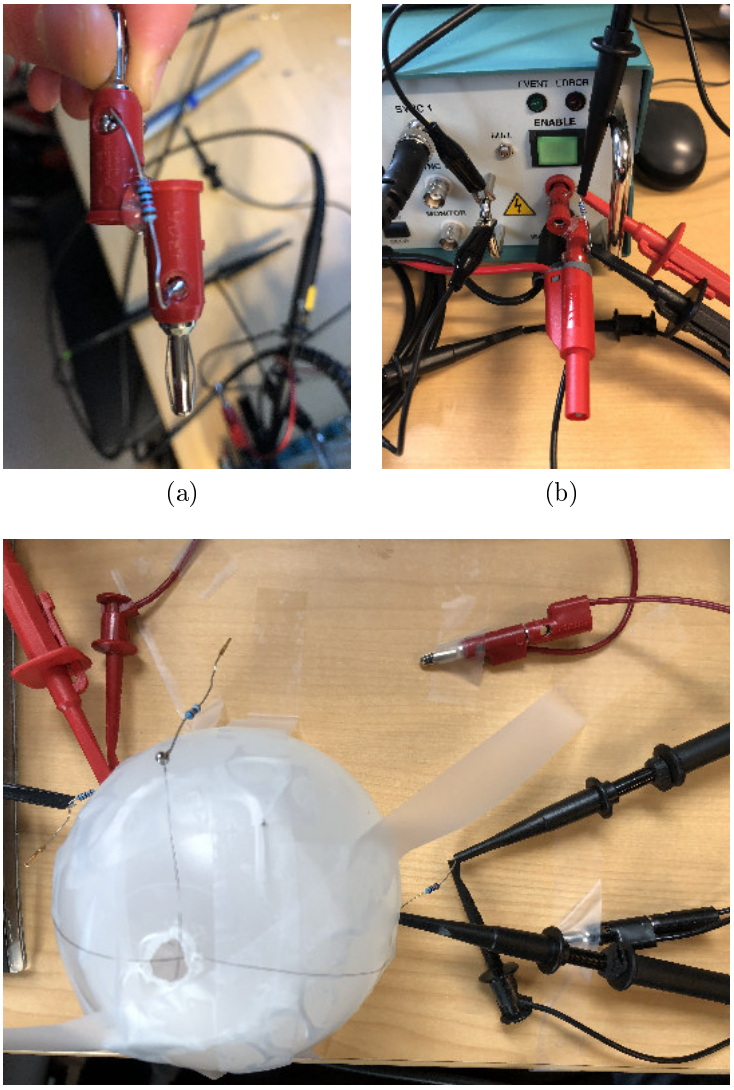

(a) (b)

(c)

Figure 3.14: Pictures of the test microstimulation measurement setup. (a) Picture of two banana plugs glued together and a 10 kΩ test resistor soldered in between. (b) Acquisition of the voltage difference on the positive output is done with a high-differential oscilloscope probe seen on the right side. The voltage on the positive and the negative output are acquired with two standard passive probes grounded to the metal handle of the stimulator. (c) Dummy brain filled with a 2 % Agarose mixture. The return tungsten wire is shown at the bottom of the right side of the picture. The other two wires show the tungsten wire / electrode connected to the signal output. Test clips are used to connect to the resistors. Voltage differences are measured with probes.

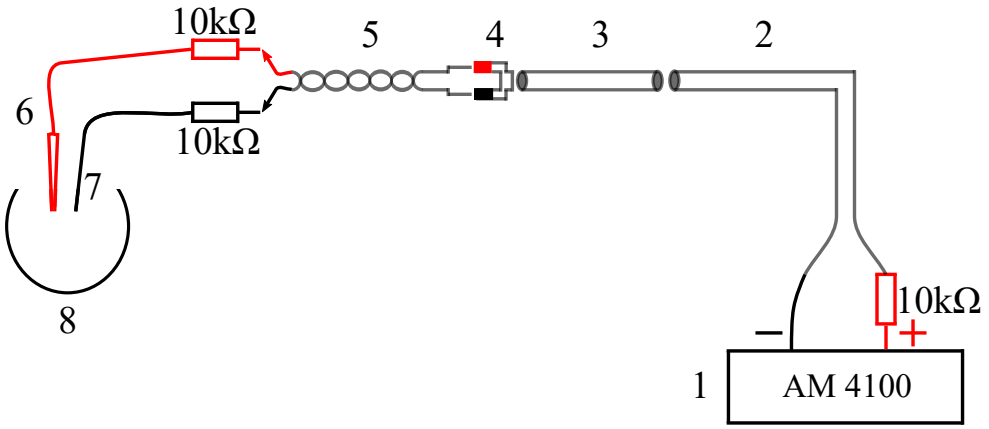

Figure 3.15: Schematic setup for doing microstimulations in a dummy brain. (1) A-M Systems Model 4100 Isolated High Power Programmable Stimulator, (2) 2 m BNC to banana test lead cable, (3) 15 ft BNC cable, (4) BNC female to dual banana plug, (5) twisted dual banana cable, (6) 400 kΩ tungsten wire / 50 kΩ to 100 kΩ microstimulation electrode, (7) tungsten reference wire, (8) dummy brain filled with a 2 % Agarose mixture.

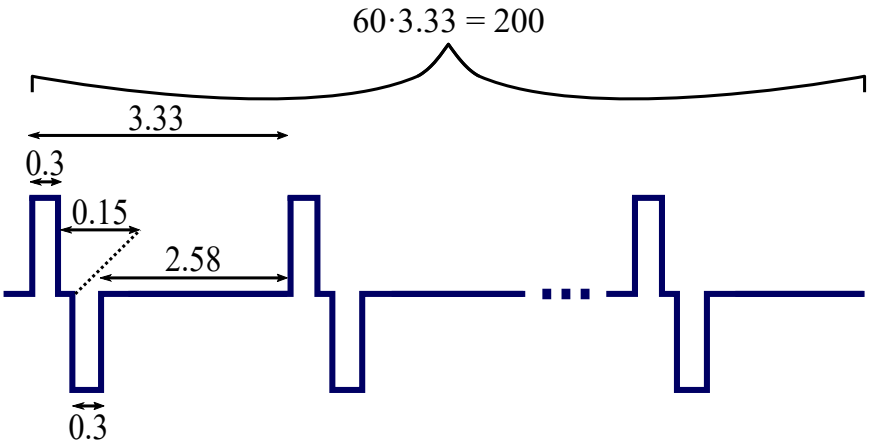

Figure 3.16: Schematic overview of ideal current pulses. 200 ms stimulation trains composed of 60 biphasic current pulses with a frequency of 300 Hz are applied in this test setup. Each biphasic pulse starts with a 0.3 ms positive phase (anodal), followed by 0.15 ms inter-phase interval and 0.3 ms negative phase. There is a 2.58 ms interval between sets of pulses resulting in a time duration of 3.33 ms per pulse.

4 Results

The following sections outline all results obtained from Chapter 3. Initially, the data recordings from the testing of various systems outside MRI environment are outlined in Section 4.1. Then, in Section 4.2 the results of recordings from two various signal sources based on the Tucker Davis system are displayed. Finally, the results of the microstimulation device testing are described in Section 4.3.

4.1 Outside MRI environment

In the following subsections the results of all three approaches characterized for broadband signal recordings outside MRI environment are listed. In Subsection 4.1.1 the results of the DAM80 are outlined. Then, in Subsection 4.1.2 and Subsection 4.1.3 the results of the Open Ephys and Tucker Davis system are given. Here, the time continuous high pass filtered spikes and low pass filtered LFPs are plotted separately and their single sided amplitude spectra are calculated. Furthermore, SNR for the spike data is estimated for each system and setup configuration. In Subsection 4.1.2 noise reduction strategies, especially for the Open Ephys system are outlined. However, strategies are also applicable for the Tucker Davis system and other electrophysiological recording setups.

4.1.1 DAM80

This setup provides a good opportunity for a fast, imprecise first characterization of the signal provided by a signal simulator. For the acquisition of the signals a low pass of 300 Hz and a high pass of 3 kHz are applied. The amplification gain is set to 100. Here, the duration of the spikes is determined to be between 300 µs and 800 µs and the amplitudes are in the range of ±400 µV which is in concordance with literature (see [17] and [28]).

4.1.2 Open Ephys

Neural data is recorded for 60 s for each of the three setup configurations described in Chapter 3.1.2. The raw data is stored in the Open Ephys format which is read into Matlab with an analysis tool. Post-processing is done by separation of the raw data in spike and LFP data with the appropriate filter settings. Spikes are obtained by using a 2^{nd} order Butter worth filter with a low cut frequency of 300 Hz and a high cut of 5 kHz and LFPs by changing the filter parameters to a low cut of 3 Hz, a high cut of 300 Hz and additionally adding a Notch of 60 Hz for removal of the line noise.

The RMS and the maximum and minimum values in µV for all setup configurations are summarized in Table 4.1. The values for the LFP data are obtained from the ungrounded setup configuration 1 only. Additionally, there are general noise reduction strategies outlined at the end of this subsection.

	Spikes				**LFP**
Configuration	1	2	3	**mean**	1
RMS [µV]	6.37	15.22	8.55	10.05	167.03
max [µV]	212.20	198.15	200.27	203.54	287.26
min [µV]	-178.13	-189.66	-184.72	-184.17	-301.81

Table 4.1: RMS = root-mean square, max = maximum, min = minimum and mean values in µV for the spikes and LFPs and all setup configurations (1, 2, 3).

Spikes

The low pass filtered spike data is shown exemplary for setup configuration 1 in Fig. 4.1. The single sided amplitude spectrum is computed in Matlab by using the fast Fourier transform (FFT). The x-axis is limited to 8000 Hz in Fig. 4.2 due to almost no signal change above this limit. Again, only setup configuration 1 is plotted here. In general, the greatest amplitude power lies in the range of 9 Hz to 1052 Hz for all setup configurations. Prominent peaks are identified at 100 Hz and its harmonics up to 1000 Hz and at 152 Hz and its harmonics up to 1064 Hz. For all three setup configurations a slightly high noise amplitude value is observed at 3300 Hz (0.14 µV to 0.25 µV), at 6614 Hz (0.04 µV to 0.07 µV) and 7500 Hz (0.05 µV to 0.06 µV). Additional noise peak values are found at 117 Hz (0.04 µV for all setup configurations) and 135 Hz (0.04 µV to 0.05 µV).

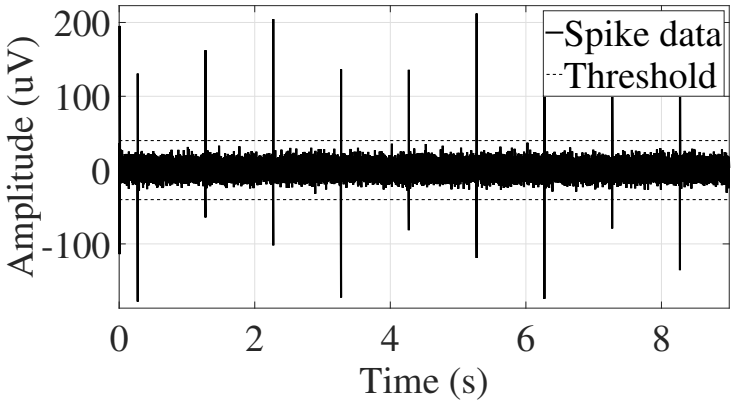

(a)

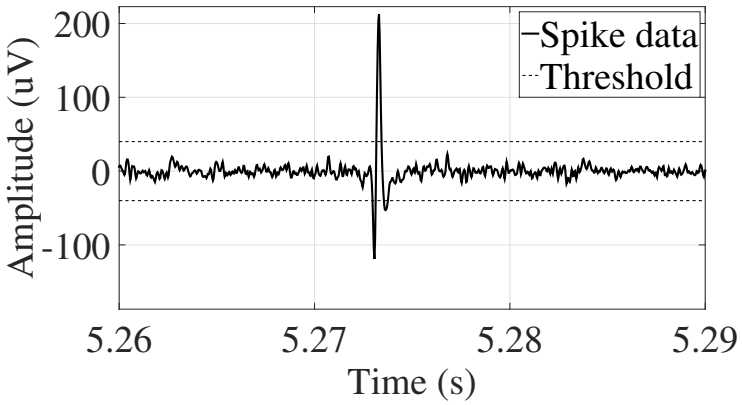

(b)

Figure 4.1: (a) Time continuous spike data. The x-axis displays the time in s and the y-axis the voltage in µV. The threshold is estimated. (b) Zoom of the spike data.

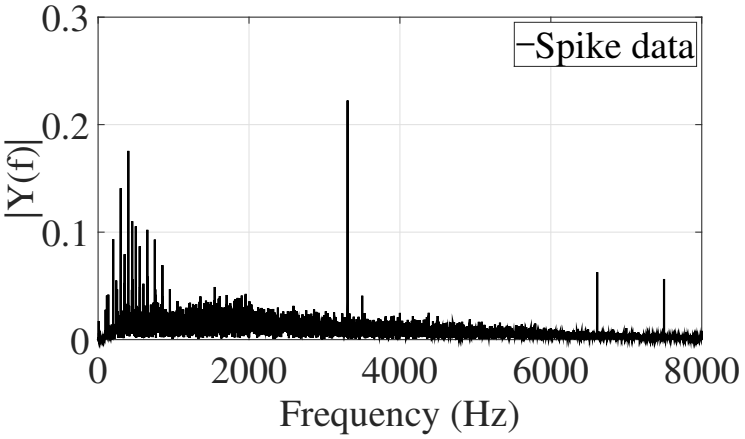

Figure 4.2: Single sided amplitude spectrum for setup configuration 1. The x-axis displays the frequency in Hz (only the first 8000 Hz are shown) and the y-axis the absolute value of the spike data amplitude in µV.

The SNR of the recorded band pass filtered spike data is calculated with Equ. 4.1

according to [61] for all three setup configurations:

$$SNR_{dB} = 20log\left(\frac{\frac{1}{N}\sum_{n=1}^{N} RMS\left(spike_n(t)\right)}{\hat{\sigma}_{noise}}\right) \tag{4.1}$$

whereby $\hat{\sigma}_{noise}$ denotes the median absolute deviation of the noise, $RMS\left(spike_n(t)\right)$ the root-mean square amplitude of a time-limited spike segment and N the number of spikes. To separate the useful signal from the noise an upper and lower threshold is set. The RMS amplitude is determined for the two signal characteristics best representing spikes. The time duration t is set to 150 ms for each spike. The SNR gives a good quality measure in regard to the size of the action potentials compared to the background noise. As the used simulator generates very large spikes in a similar amplitude range compared to the background noise, good SNR values are achieved in this study. Results are summarized in Table 4.2.

Setup c.	**t_low [µV]**	**t_high [µV]**	**SNR_low [dB]**	**SNR_high [dB]**	**SNR_mean [dB]**
1	-40	40	57.7	59.6	58.2
2	-90	90	48.5	49.3	48.9
3	-50	50	53.0	53.3	53.2

Table 4.2: Summary of threshold and calculated SNR values of three different setup configurations. Setup c. = Setup configuration, t_low = lower threshold, t_high = higher threshold, SNR = signal-to-noise ratio.

LFP

The LFP signal consists of two superimposed sine waves with 3 Hz and 9 Hz and is shown in Fig. 4.3. Its single sided amplitude spectrum is displayed in Fig. 4.4 for setup configuration 1. The two peaks at 3 Hz with an amplitude of 15.60 µV and 9 Hz with an amplitude of 20.98 µV can be clearly seen. Additional peaks can be observed especially in the low frequency range <100 Hz, 117 Hz (0.29 µV) and 135 Hz (0.22 µV). However, all of those additional noise peaks are by magnitudes smaller compared to the amplitude power of the useful signal.

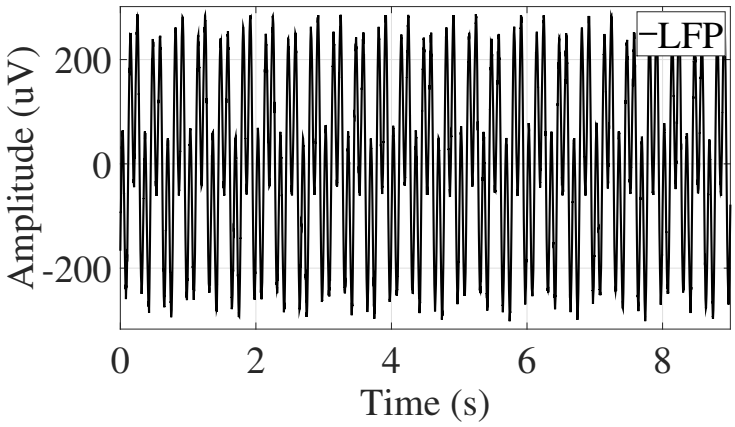

Figure 4.3: LFP signal of setup configuration 1. The x-axis displays the time in s and the y-axis the voltage in µV.

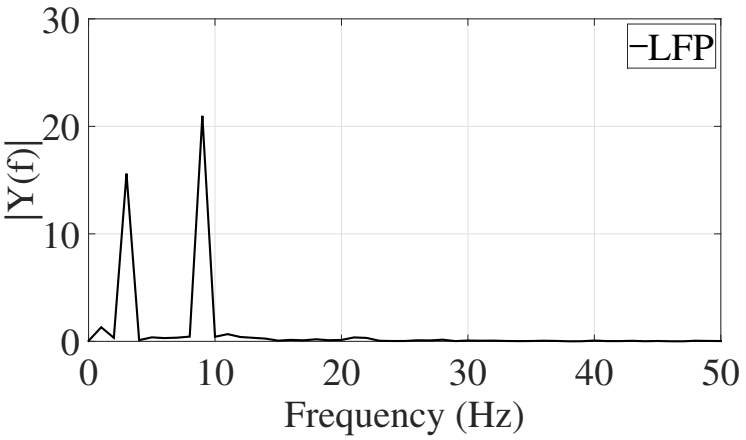

Figure 4.4: Single sided amplitude spectrum. The x-axis displays the frequency in Hz (only the first 50 Hz are shown) and the y-axis the absolute value of the amplitude in µV.

General noise reduction strategies

In order to reduce noise in the data acquisition, different noise reduction strategies are developed and applied in the previously described measurements:

1. Wire adapter
   a) cut of all unused wires as short as possible,
   b) twist, solder and ground of unused wired to the Faraday cage and
   c) solder of signal wire to alligator clip and reference wires to mini banana plug-in for a good connection to the signal generator
2. Use of a desktop PC instead of a laptop (it has been found that the floating ground of the laptop is more sensitive to line noise)

3. Ground of the outer shell of the USB cable that connects the acquisition board to the PC and ground of acquisition board itself
4. Shielding of single wires with aluminum foil
5. Use of a Faraday cage made of aluminum foil
6. Connection of the acquisition board and the PC to the same earth ground

4.1.3 Tucker Davis

Data is recorded for 60 s and stored in the TDT data tank format which is a special directory on the hard drive. The low and high pass filtered spikes and LFP data according to the parameters in 3.1.3 are directly loaded into Matlab from the software Synapse. The RMS, maximum and minimum values for the frequency separated raw data in spikes and LFP are summarized in Table 4.3.

	Spikes	**LFP**
RMS [µV]	6.19	171.44
max [µV]	201.73	328.49
min [µV]	193.85	-337.55

Table 4.3: RMS = root-mean square, max = maximum, min = minimum values in µV for the spikes and LFPs.

Spikes

The low pass filtered spike data is displayed in Fig. 4.5 and its single sided amplitude spectrum respectively in Fig. 4.6. The most prominent peak is at 491 Hz (0.24 µV) which is assumed to be the frequency of the signal. Further peaks are at 117 Hz (0.05 µV), 135 Hz (0.05 µV) and 1501 Hz (0.05 µV).

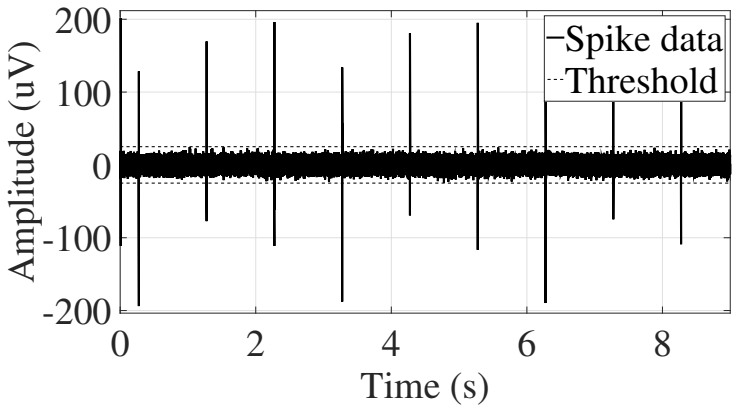

(a)

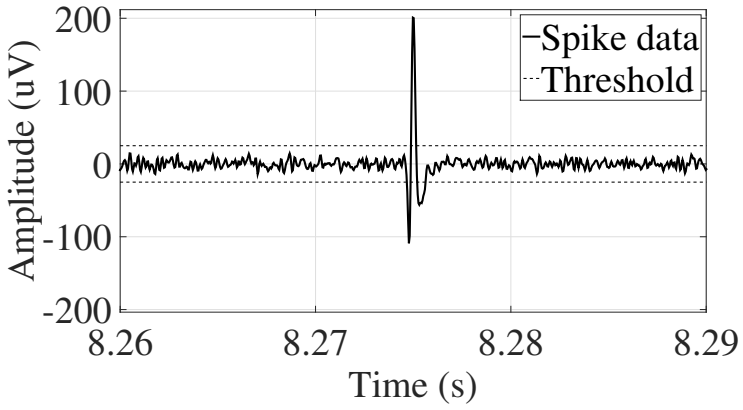

(b)

Figure 4.5: a) Time continuous spike data. The x-axis displays the time in s and the y-axis the voltage in µV. The threshold is estimated. (b) Zoom of the spike data.

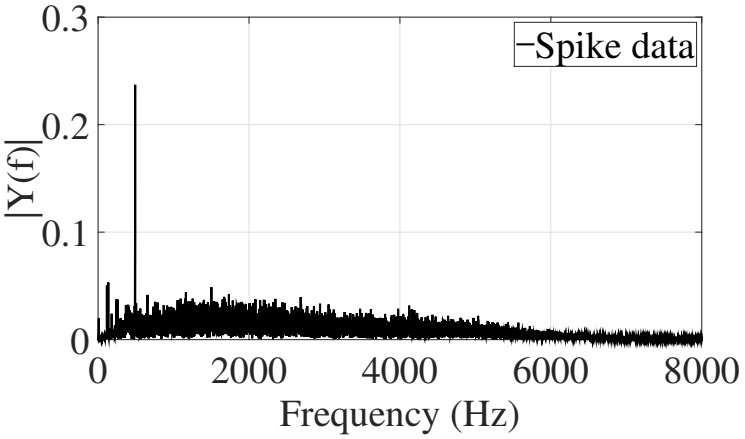

Figure 4.6: Single sided amplitude spectrum. The x-axis displays the frequency in Hz (only the first 8000 Hz are shown) and the y-axis the absolute value of the amplitude in µV.

The SNR of the spike signal is determined using Equ. 4.1. The threshold is set

to ±25 µV. Again, the SNR value is determined for two representative spikes in the signal. Results are summarized in Table 4.4.

t_low [µV]	**t_high [µV]**	**SNR_low [dB]**	**SNR_high [dB]**	**SNR_mean [dB]**
-25	25	60.9	61.1	60.0

Table 4.4: Summary of threshold and calculated SNR values. t_low = lower threshold, t_high = higher threshold, SNR = signal-to-noise ratio.

LFP

The LFP signal is plotted in Fig. 4.7a and the single sided amplitude spectrum in Fig. 4.7b. As most of the spectral power lies within the first 50 Hz and to obtain a higher resolution only this frequency segment is displayed. It is verified again here that the LFP signal of the signal generator consists of two superimposed sine waves at 3 Hz (15.91 µV) and 9 Hz (21.61 µV). Prominent noise peaks are again in the low frequency range <100 Hz and at 117 Hz (0.33 µV) and 135 Hz (0.27 µV).

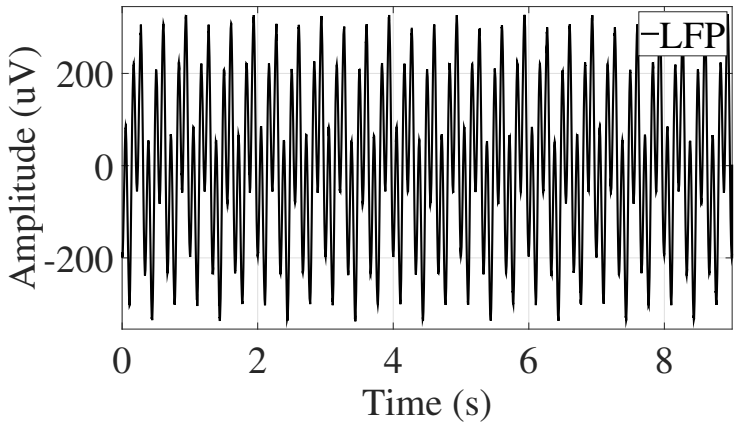

(a)

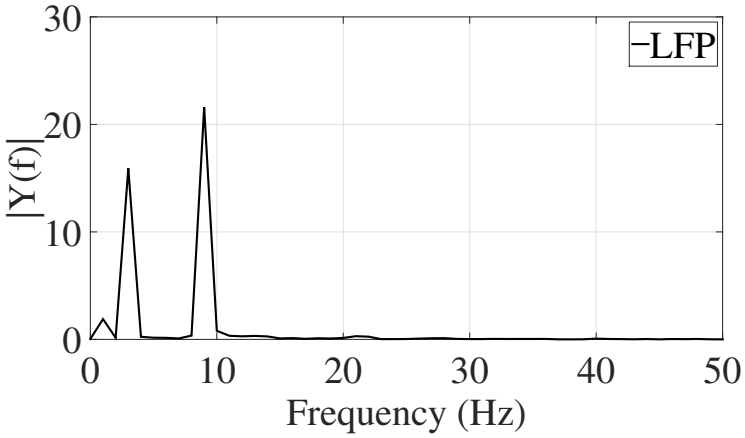

(b)

Figure 4.7: (a) LFP signal. The x-axis shows the time in s and the y-axis the amplitude in µV. (b) Single sided amplitude spectrum. The x-axis displays the frequency in Hz (only the first 50 Hz are shown) and the y-axis the absolute value of the amplitude.

4.2 Inside MRI environment

In the following chapter the results for Subsection 3.2.1 and Subsection 3.2.2 are summarized. Subsection 4.2.1 outlines the results for the function generator recordings in the control room, the static magnetic field only and during a scan. The same chapter division is done for the recordings with a single resistor as signal source in Subsection 4.2.2.

4.2.1 Broadband signal recordings

In each environment / for each condition five recordings, each lasting around 60 s are done. Sine waves with five different fundamental frequencies
(10 Hz, 100 Hz, 500 Hz, 1000 Hz and 2000 Hz) and an amplitude of around 600 µV are generated with a function generator. As in Subsection 4.1.3 data is stored in the

TDT data tank format and then loaded into Matlab.

Baseline

The time signal of the sine wave with a fundamental frequency of 100 Hz is displayed exemplary for a time period of around 190 ms in Fig. 4.8a and its single sided amplitude spectrum in Fig. 4.8b. A power of 9.04 µV is verified at 100 Hz. Noise components are primarily caused by the 60 Hz net frequency. The most prominent noise peak is at one of its harmonics, 720 Hz, with a peak amplitude of 0.20 µV.

Data of sine waves with different fundamental frequencies is analyzed with respect to its RMS, maximum and minimum values which are summarized in Table 4.5.

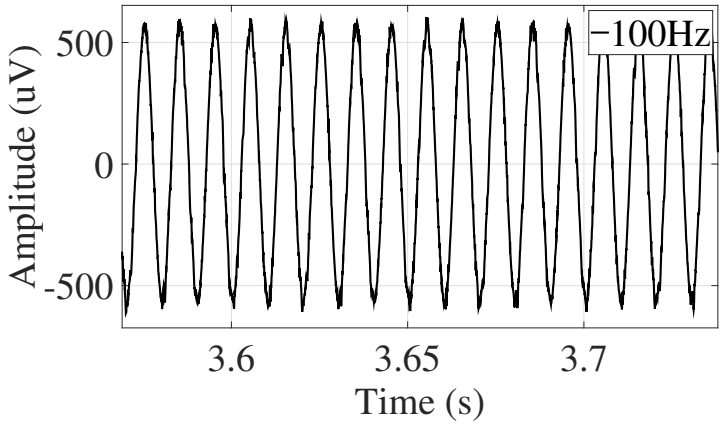

(a)

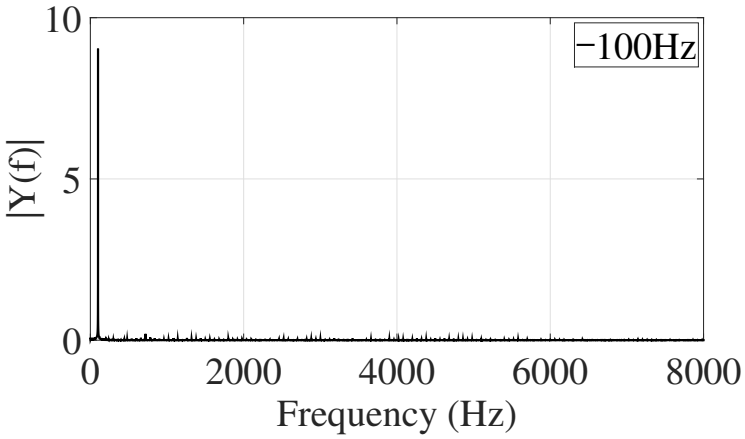

(b)

Figure 4.8: (a) Sine wave with a fundamental frequency of 100 Hz and and an amplitude of around 600 µV recorded in the control room. The x-axis shows the time in s and the y-axis the amplitude of the signal in µV. (b) Single sided amplitude spectrum. The x-axis displays the frequency in Hz (only the first 8000 Hz are shown) and the y-axis the absolute value of the amplitude.

Frequency [Hz]	10	100	500	1000	2000	**mean**
RMS [µV]	401.86	401.32	398.78	399.30	400.81	400.41
max [µV]	627.07	621.57	613.18	617.86	617.34	619.40
min [µV]	-646.72	-641.73	-1359.70	-640.00	-644.86	-786.61

Table 4.5: RMS = root-mean square, max = maximum, min = minimum and mean values in µV for all fundamental frequencies (10 Hz, 100 Hz, 500 Hz, 1000 Hz and 2000 Hz) recorded in the control room.

Static magnetic field

We recorded data in the static magnetic field B_o. The time signal and single sided amplitude spectrum of the sine wave with a fundamental frequency of 100 Hz are displayed in Fig. 4.9. In Fig. 4.9b it is shown that the fundamental frequency of the signal again results in the highest amplitude power with a value of 9.01 µV. As previously mentioned, noise sources in the amplitude spectrum are caused by the 60 Hz net frequency and its harmonics. The most significant noise peak is, as in 4.2.1, identified at 720 Hz and also has a similar amplitude of 0.31 µV.

The single sided amplitude spectrum in Fig. 4.9b suggests that low frequency noise is caused by the static magnetic field B_o. Thus, in Fig. 4.9c the amplitude spectrum is zoomed. To verify this assumption across all measurements noise peaks from the amplitude spectra with values >0.10 µV are listed in Table 6.1 and Table 6.2 in the Attachment. Remarkable noise peaks across measurements are identified between 14 Hz and 60 Hz and also at 720 Hz and 840 Hz. Especially high noise peaks are obtained at 41 Hz (0.84 µV to 1.45 µV) and 43 Hz (1.52 µV to 2.21 µV).

Moreover, data for all fundamental frequencies is analyzed again with respect to its RMS, maximum and minimum values (see Table 4.6). The RMS value is increased by around 6 % compared to the baseline measurement as previously described, the maximum values are increased by the factor 2.2 and the minimum amplitude values by the factor 1.7 on the average.

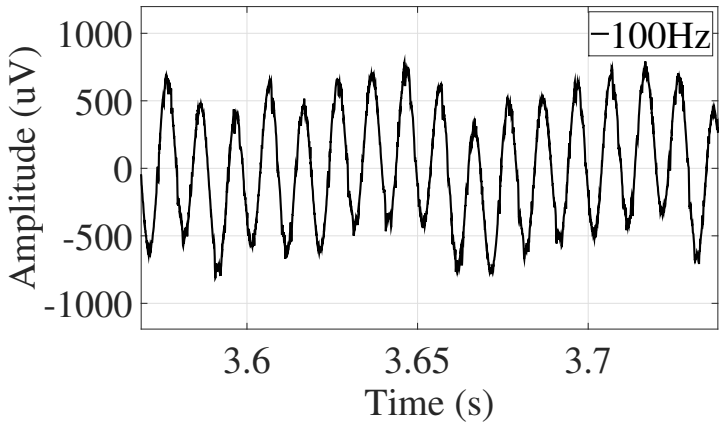

(a)

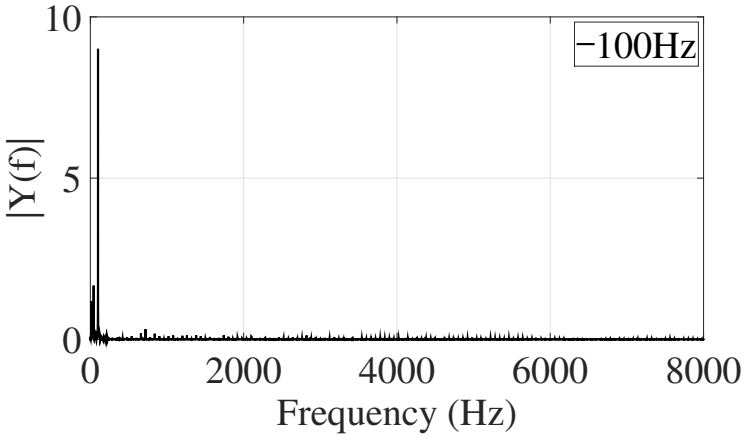

(b)

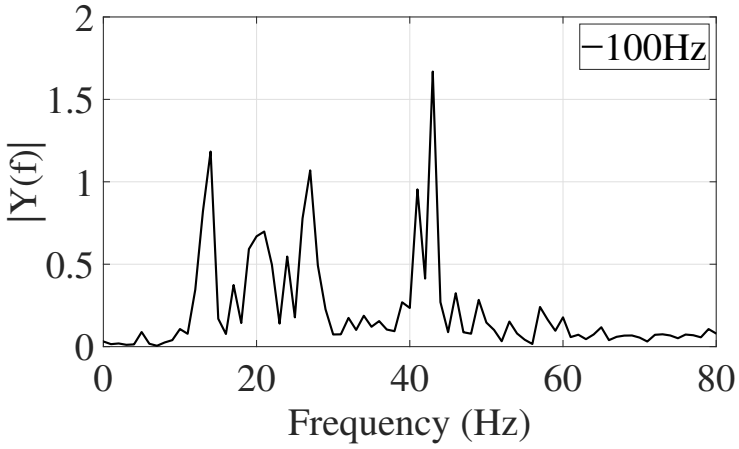

(c)

Figure 4.9: (a) Sine wave with a fundamental frequency of 100 Hz and an amplitude of around 600 µV recorded in the static magnetic field. The x-axis shows the time in s and the y-axis the amplitude of the signal in µV. (b) Single sided amplitude spectrum. The x-axis displays the frequency in Hz (only the first 8000 Hz are shown) and the y-axis the absolute value of the amplitude. (c) Zoom of the single sided amplitude spectrum.

Frequency [Hz]	10	100	500	1000	2000	**mean**
RMS [µV]	427.22	425.13	428.28	424.50	425.76	426.18
max [µV]	2655.40	1140.70	1080.10	1107.30	1076.80	1412.10
min [µV]	-1352.60	-1134.10	-1100.90	-1162.70	-1169.90	-1184.10

Table 4.6: RMS = root-mean square, max = maximum, min = minimum and mean values in µV for all fundamental frequencies (10 Hz, 100 Hz, 500 Hz, 1000 Hz and 2000 Hz) recorded in the static magnetic field.

Scan

We performed a scan with an EPI sequence with the manufacturers standard's parameter settings and recorded data. In Fig. 4.10 the fMRI gradient artefacts are shown. The overall scan time is 60 s and the acquisition of one volume takes 2.25 s (see Fig. 4.10a). One volume consists of 45 slices. Each slice has a repetition time of 50 ms and the time delay for switching to the next volume is 40 µs. A single slice gradient artefact is shown in Fig. 4.10b. A couple of time-events related to the EPI pulse sequence are labeled. The acquisition of one slice starts with the slice selection gradient. The readout gradient with a high switching frequency of 646 Hz is sine modulated with changing polarity. Crushers at the end of the sequence are used as correction gradients to remove any remaining unwanted magnetization.

Figure 4.11 shows the single sided amplitude spectrum of the fMRI gradient artefact. Discrete noise amplitude peaks are at 20 Hz which is the inverse of the slice repetition time and its harmonics. Furthermore, significant peaks are found at the volume acquisition frequency and at the gradient switching frequency (646 Hz). A slight inaccuracy in the harmonics of the slice repetition frequency artefact is caused by the fact that the MRI scanner and the Tucker Davis system are operated by separate clocks, which causes a time drift. This effect is also observed in [41].

The value of the frequency of the true signal increases to 84.97 µV which is around 90 times higher than the amplitude power observed in the baseline and static magnetic field recordings. However, due to the fact that 100 Hz is also a harmonic of the slice repetition frequency, this quantification might not be exact. An increase in amplitude power of the EEG signal measurement of up to 100 times compared to the true signal has also been observed elsewhere (see [41]).

Again, data for all fundamental frequencies is analyzed with respect to its RMS, maximum and minimum values which are summarized in Table 4.3. RMS values are on the average 600 times higher than the true value observed in the baseline recordings. Maximum and minimum amplitudes are up to 900 times higher compared to the values observed in the baseline and static magnetic field recordings. The maximum and minimum amplitude values are above the voltage range of the pre-amplifier, which means that it is saturated.

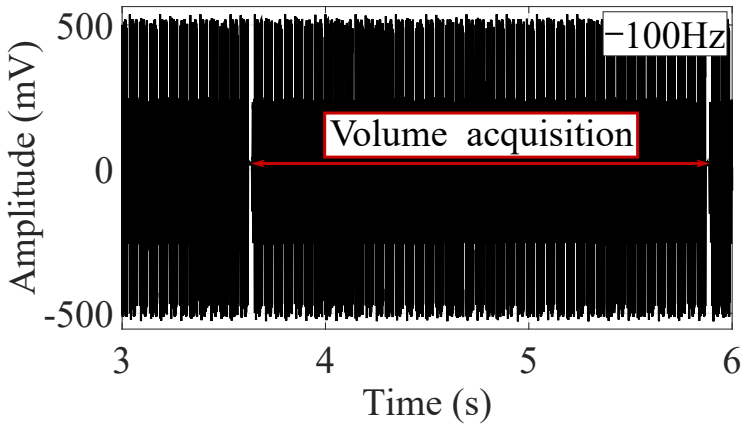

(a)

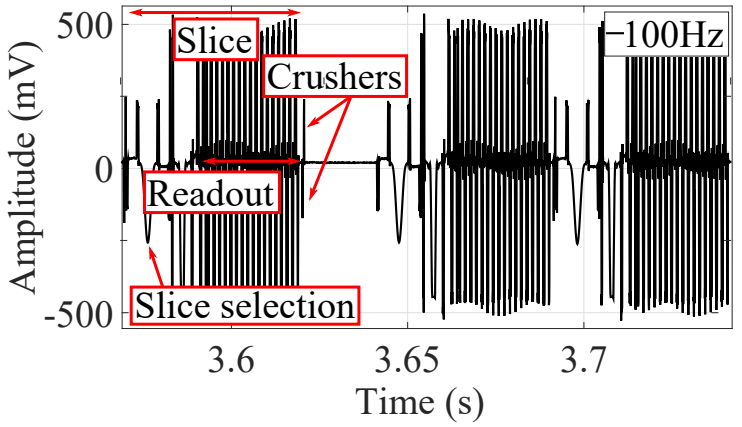

(b)

Figure 4.10: (a) Gradient artefact of a 100 Hz sine wave with an amplitude of around 500 mV. The x-axis shows the time in *s* and the y-axis the amplitude of the signal in mV. The volume acquisition time is indicated. (b) Single slice gradient artefact. Some features related to the EPI sequence are outlined. The x-axis shows the time in s and the y-axis the amplitude of the signal in mV.

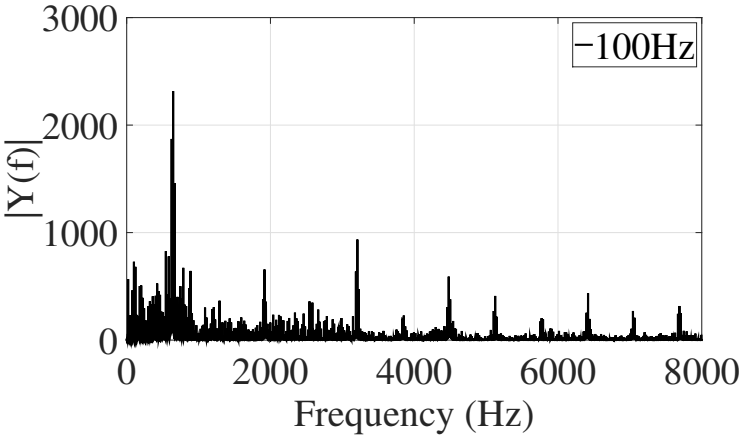

Figure 4.11: Single sided amplitude spectrum of the 100 Hz sine wave. The x-axis displays the frequency in Hz (only the first 8000 Hz are shown) and the y-axis the absolute value of the amplitude.

Frequency [Hz]	10	100	500	1000	2000	**mean**
RMS [mV]	241.63	243.18	242.57	242.09	242.14	242.32
max [mV]	536.87	536.87	536.87	536.87	536.87	536.87
min [mV]	-528.83	-528.41	-528.65	-528.49	-528.65	-528.61

Table 4.7: RMS = root-mean square, max = maximum, min = minimum and mean values in mV for all fundamental frequencies (10 Hz, 100 Hz, 500 Hz, 1000 Hz and 2000 Hz) recorded during an fMRI scan.

4.2.2 Noise estimation

As in Subsection 4.2.1 in each environment / for each condition recordings lasting for 60 s are done and repeated five times. Compared to 4.2.1 a 930 kΩ resistor is used as signal source for mimicking brain resistance.

Baseline

We recorded data in the control room to get a baseline data set. The time signal of the pure noise segment of one measurement is displayed exemplary for the whole acquisition time in Fig. 4.12a. The noise threshold is estimated to be ±75 µV. A zoom of 0.02 s of the time signal is shown in Fig. 4.12b to demonstrate the signal shape in more detail.

The single sided amplitude spectrum is calculated respectively and shown in Fig. 4.13. No significant noise frequency peaks are identified. A slightly high amplitude of 0.012 µV is observed at 0 Hz. This DC offset is caused by the setting AC coupling in the pre-amplifier and can be simply eliminated by changing the setting to DC coupling. Data for all recordings is analyzed with respect to its RMS, maximum, and minimum value, summarized in Table 4.5.

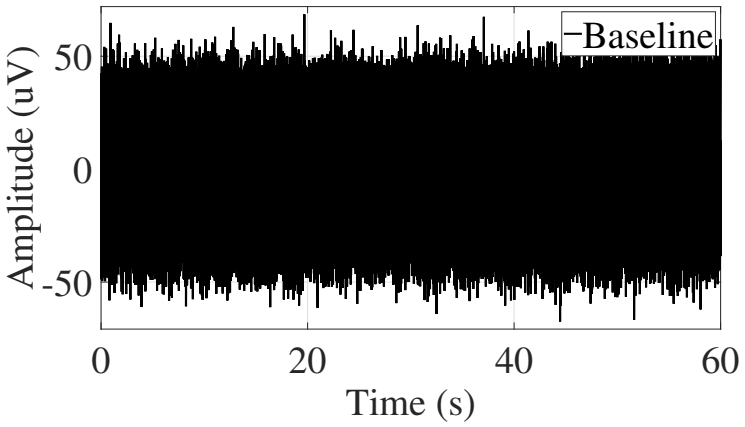

(a)

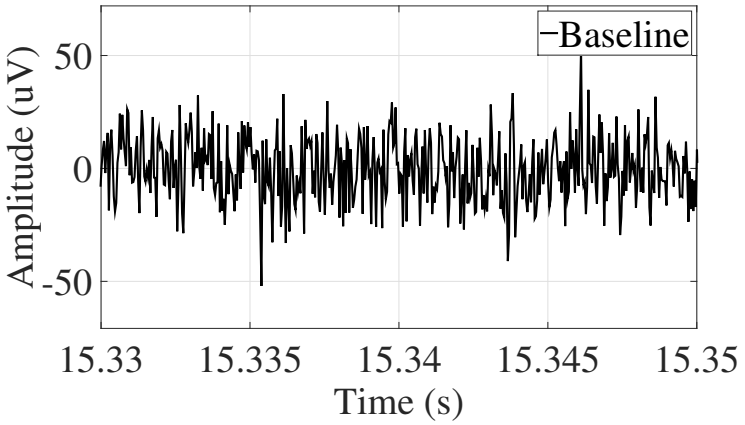

(b)

Figure 4.12: (a) Time signal of the pure noise recorded in the control room. The x-axis shows the time in s and the y-axis the amplitude of the signal in µV. (b) Zoom of the time signal.

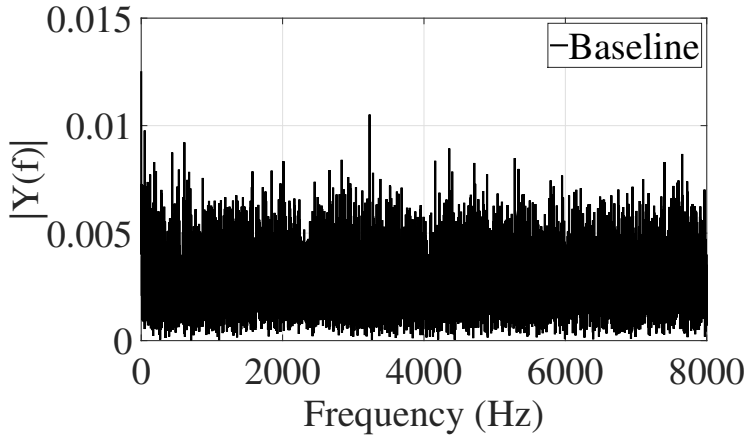

Figure 4.13: Single sided amplitude spectrum. The x-axis displays the frequency in Hz (only the first 8000 Hz are shown) and the y-axis the absolute value of the amplitude.

Measurement	1	2	3	4	5	**mean**
RMS [µV]	14.14	14.16	14.14	14.14	14.14	14.14
max [µV]	74.88	71.42	68.54	71.94	69.50	71.26
min [µV]	-66.43	-86.72	-67.46	-66.24	-72.64	-71.97

Table 4.8: RMS = root-mean square, max = maximum, min = minimum and mean values in µV for all measurements recorded in the control room.

Static magnetic field

Data is recorded in the static magnetic field B_o. The signal for the complete recording time is shown in Fig. 4.14a and a time extract of 0.02 s in Fig. 4.14b. The noise threshold is estimated to be at ±85 µV.

The single sided amplitude spectrum is displayed in Fig. 4.15 respectively. As in Subsection 4.2.1 the amplitude spectrum leads to the assumption that low frequency noise is caused by interference with the static magnetic field.

For verification of this suggestion, again, peak amplitudes from the amplitude spectrum with a value >10.00 nV are evaluated and subsequently listed in Table 6.3 and Table 6.4 in the Attachment. Here, the peak detection threshold in the amplitude spectrum is lowered by the factor 10 compared to Subsection 4.2.1. Prominent noise peaks are observed at 41 Hz, 43 Hz, 49 Hz and 98 Hz. Again, as in Subsection 4.2.1 the highest frequency noise peaks are identified at 41 Hz, with an amplitude between 11.10 nV and 16.24 nV and at 43 Hz, with an amplitude between 16.29 nV and 26.42 nV.

Also, data for all measurements is analyzed with respect to its RMS, maximum, and minimum values (see Table 4.9). As in Subsection 4.2.1 the RMS value increases by 6 % on the average. The maximum and minimum amplitude values are more stable and only increase by 8 % and 3 % on the average.

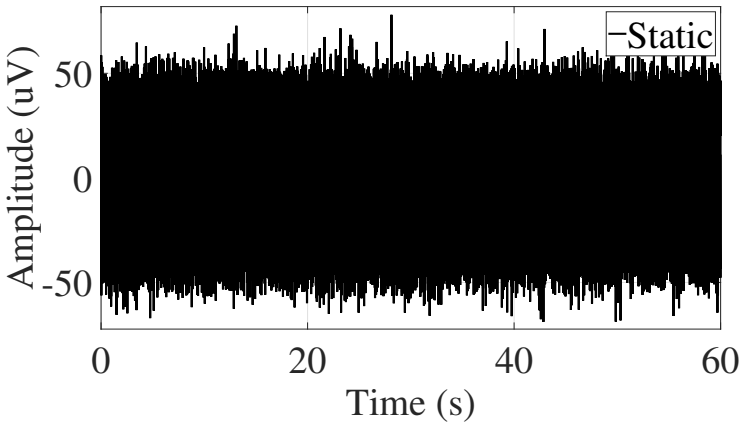

(a)

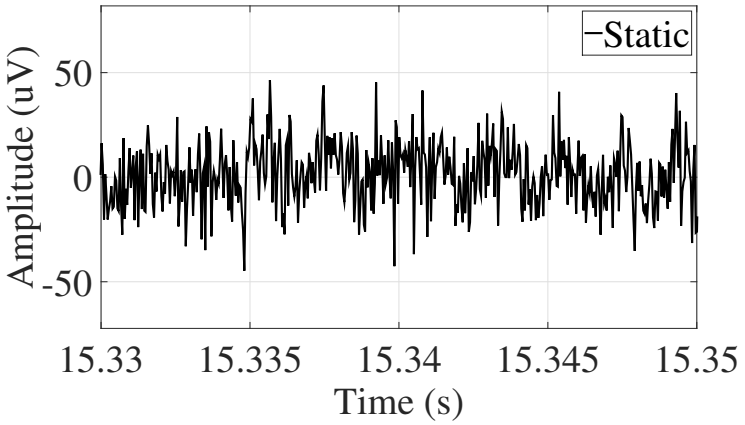

(b)

Figure 4.14: (a) Time signal of the noise recorded in the static magnetic field. The x-axis shows the time in s and the y-axis the amplitude of the signal in µV. (b) Zoom of the signal.

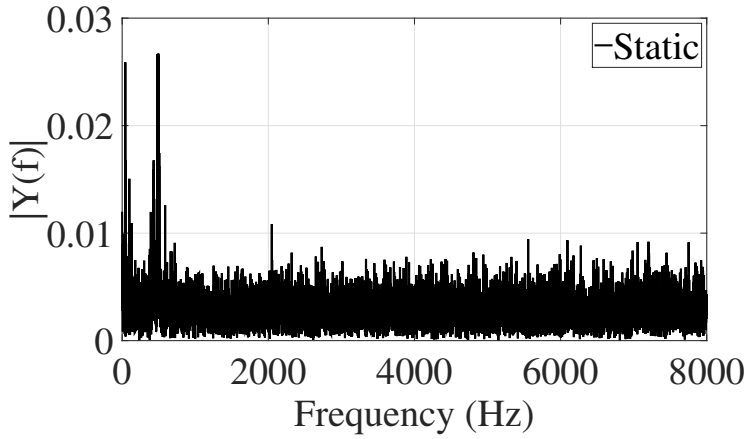

Figure 4.15: Single sided amplitude spectrum. The x-axis displays the frequency in Hz (only the first 8000 Hz are shown) and the y-axis the absolute value of the amplitude.

Measurement	1	2	3	4	5	**mean**
RMS [µV]	15.02	14.93	15.00	15.16	15.21	15.07
max [µV]	71.62	78.02	76.80	80.26	81.09	77.56
min [µV]	-75.46	-68.86	-73.66	-73.92	-78.34	-74.04

Table 4.9: RMS = root-mean square, max = maximum, min = minimum and mean values in µV for all measurements recorded in the static magnetic field.

Scan

We performed a scan with an EPI sequence and recorded electrophysiological data. In Fig. 4.16 the fMRI gradient artefacts and the trigger signals which indicate the acquisition of a new volume block are shown.

The time onsets for polarity change of the trigger are indicated with red arrows in the upper plot of Fig. 4.16. The related trigger signal is shown below. The trigger output is between 0 V to 1 V and the time duration for one polarity is 2.25 s, which corresponds to the volume acquisition time. The time needed for the trigger to change its polarity is 40 µs.

A zoom of the gradient artefact is shown in Fig. 4.17. The related features to the applied EPI sequence are labeled. Initially, the slice selection is done. Then the readout gradient is applied. A larger distance between two EPI sequences indicates the acquisition of a new volume. The trigger signal showing the onset of a new volume is displayed below.

Fig. 4.18 plots the single sided amplitude spectrum of the fMRI gradient artefact. Again, the most prominent amplitude peaks are at the slice acquisition frequency of 20 Hz and its harmonics. Inaccuracy in the harmonics of this frequency is caused by the reasons discussed in 4.2.1. Additionally, peaks are identified at the volume acquisition frequency (0.44 Hz) and at the gradient switching frequency (646 Hz).

Moreover, data for all frequencies is analyzed with respect to its RMS, maximum and minimum values which are summarized in Table 4.10. RMS values are 9700 times higher on the average than the initial value observed previously in this subsection. Maximum and minimum amplitudes are up to 6900 times higher respectively.

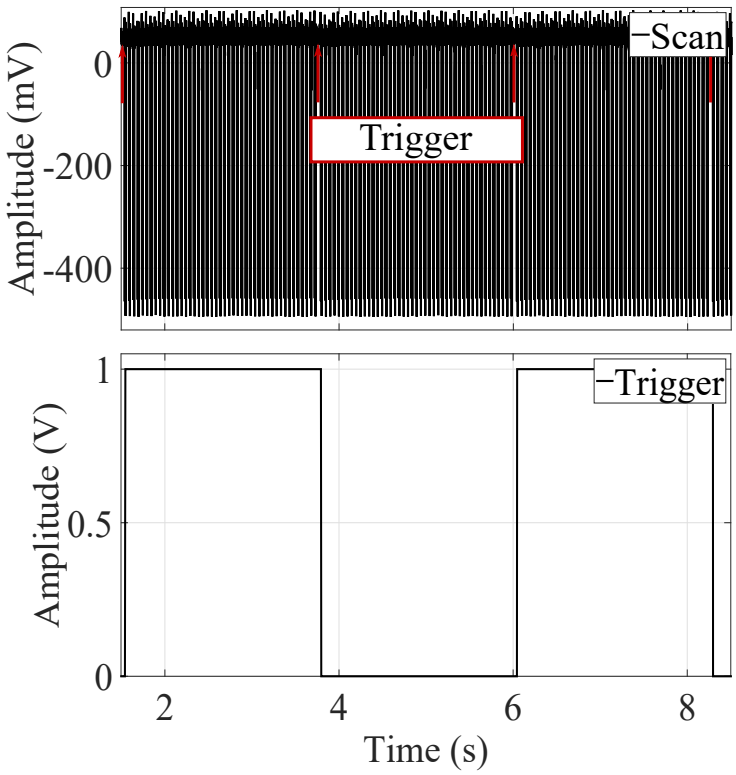

Figure 4.16: Upper plot: Gradient artefact of the pure noise segment. The onset of the trigger indicating the acquisition of a new volume is shown with red arrows. The x-axis shows the time in s and the y-axis the amplitude of the signal in mV. Lower plot: Trigger output signal for the given time range. The x-axis shows the time in s and the y-axis the amplitude of the signal in V.

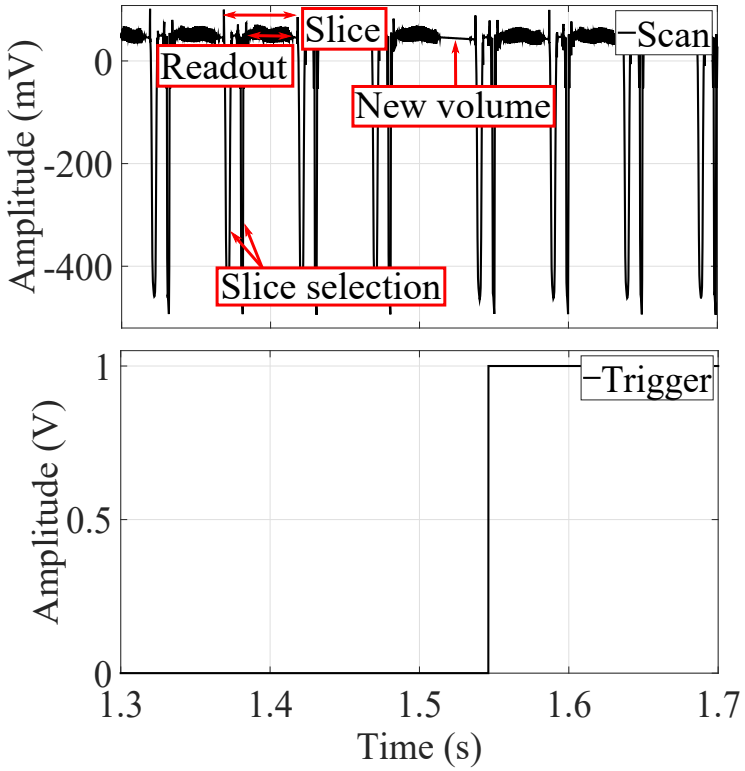

Figure 4.17: Upper plot: Zoom of the gradient artefact. Some features related to the EPI sequence are outlined. The x-axis shows the time in s and the y-axis the amplitude of the signal in mV. Lower plot: Trigger output for the given time range. The x-axis shows the time in s and the y-axis the amplitude of the signal in V.

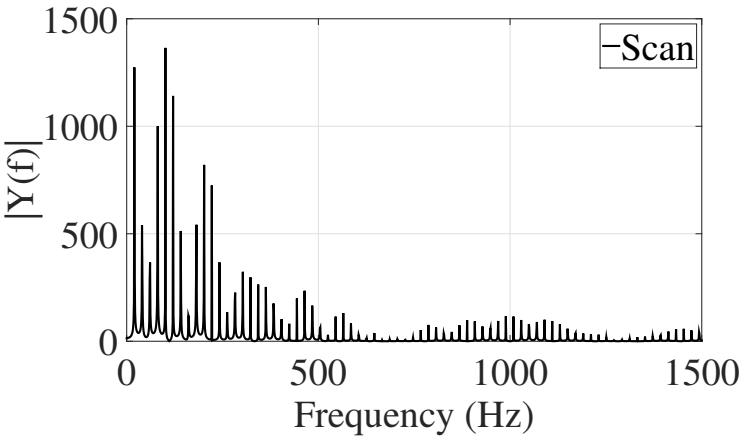

Figure 4.18: Single sided amplitude spectrum of the gradient artefact. The x-axis displays the frequency in Hz (only the first 1500 Hz are shown) and the y-axis the absolute value of the amplitude.

Measurement	1	2	3	4	5	**mean**
RMS [mV]	137.20	137.18	136.81	137.10	136.92	137.04
max [mV]	103.14	103.14	102.86	103.10	102.95	103.00
min [mV]	-495.94	-497.12	-495.59	-495.95	-495.9	-495.92

Table 4.10: RMS = root-mean square, max = maximum, min = minimum and mean values in mV for all measurements recorded during an fMRI scan.

4.3 Microstimulation

As mentioned earlier the setup is tested initially with a 400 kΩ tungsten wire and later on with a 50 kΩ to 100 kΩ microstimulation electrode. Results for the voltage of the positive and negative output of the microstimulator, trigger and stimulus currents measured at three different positions are shown in Fig. 4.19 and Fig. 4.20. The voltage of the positive output (20 V per division) of the stimulator is shown in yellow. The Vp^+ varies between 56.2 V and 73.0 V and the Vp^- between −45.7 V and −51.2 V respectively. The zero voltage of the negative output is displayed in green. The stimulus currents measured at three different positions (directly at the output of the stimulator, at the tungsten wire / electrode and the indifferent return wire end) are shown in orange. The display scaling is 100 mV per division in horizontal direction. 1 mV corresponds to a current of 1 µA. The trigger mode free run is set. 5 V per division are shown and its level displayed in purple is −18.8 V. The display scaling in the vertical direction is 1 ms per division for all channels.

In Fig. 4.19 results for the 400 kΩ tungsten wire are shown. In Fig. 4.19a the current pulses measured as voltage difference at the 10 kΩ test resistor directly at the output of the stimulator is shown. The stimulus has a Vpp^+ of 574 mV which corresponds to a current of 574 µA. In Fig. 4.19b the current measured at the 10 kΩ test resistor before the tungsten wire is shown. The Vpp^+ diminished to a value of 303 mV (corresponding to a current of 303 µA) which is around 53 % of the original value. The shape of the current has changed due to capacitive properties of the cables. In Fig. 4.19c the stimulus current at the test resistor before the return tungsten wire is acquired. A value of 283 mV is measured for the peak-to-peak voltage, which is 49 % of the original value. The shape of the stimulus current is similar to 4.19b.

In a next step the tungsten wire is replaced by a microstimulation electrode. Results are shown in Fig. 4.20. In Fig. 4.20a the stimulus current measured at the 10 kΩ test resistor directly at the output of the stimulator is displayed. A Vpp^+ of 578 mV equivalent to a current of 578 µA is identified. The stimulus current measured at the test resistor of the positive output is shown in Fig. 4.20b. The value of the peak-to-peak voltage decreases to 354 mV (61 % of the original value). Again, the shape of the current changes due to capacitive properties of the cables. In Fig. 4.20c the stimulus current measured at the negative end is shown. The Vpp^+ additionally decreases (311 mV, 54 % of the original value). All Vpp^+ values equivalent to the stimulus current are summarized in Table 4.11.

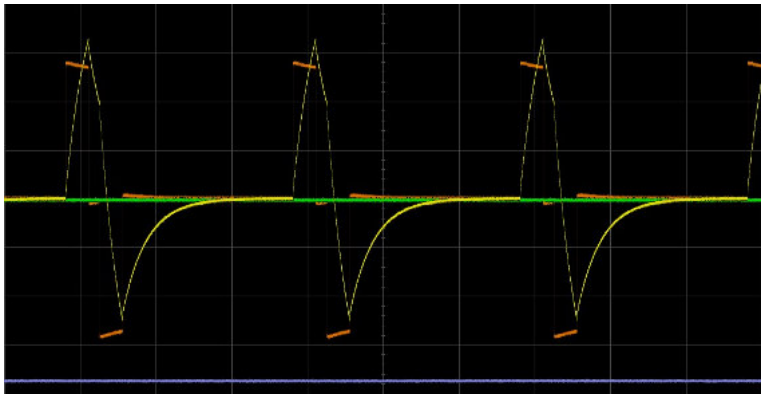

(a)

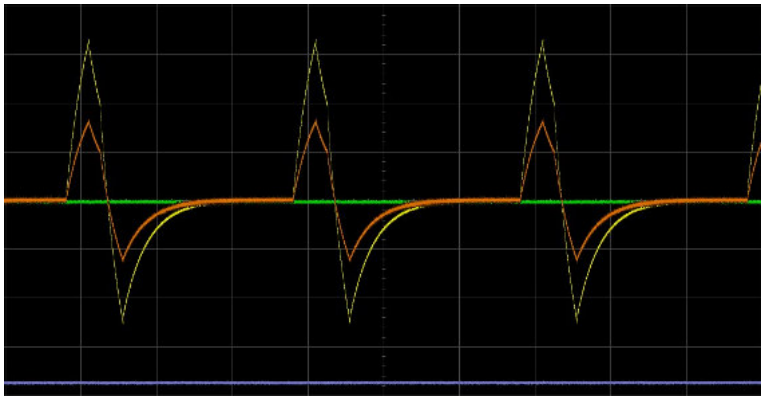

(b)

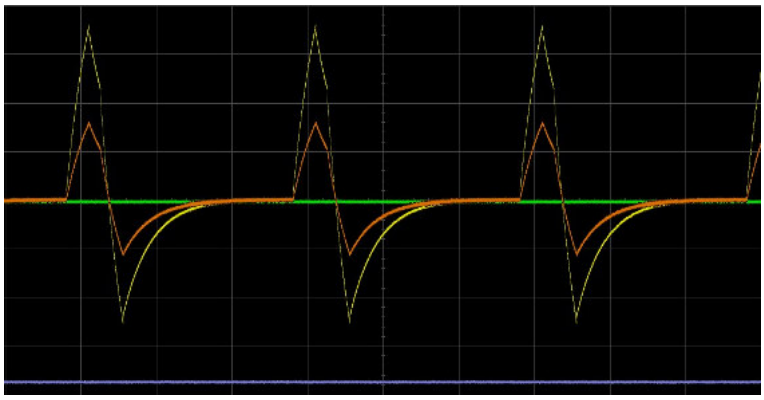

(c)

Figure 4.19: Voltage of the positive and negative output, trigger and stimulus currents measured at three different positions for a 400 kΩ tungsten wire. Yellow: Voltage of the positive output (20 V per division), Green: Voltage of the negative output (20 V per division), Orange: Stimulus current (100 mV per division equivalent to 100 µA per division), Purple: Trigger (5 V per division), Time axis: 1 ms per division. Stimulus current measured at (a) the output, (b) the positive end, (c) the negative end.

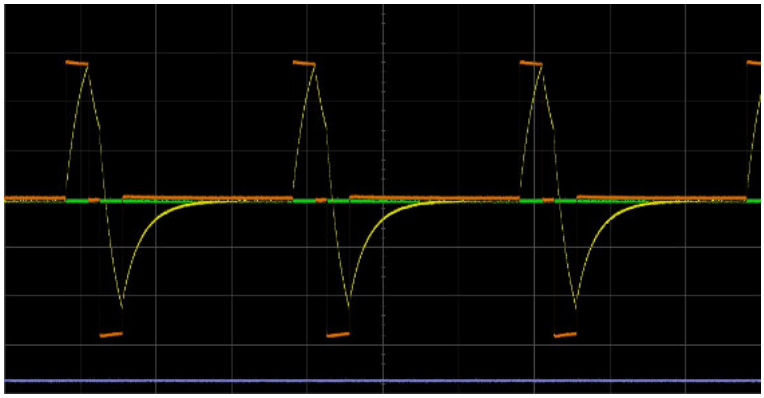

(a)

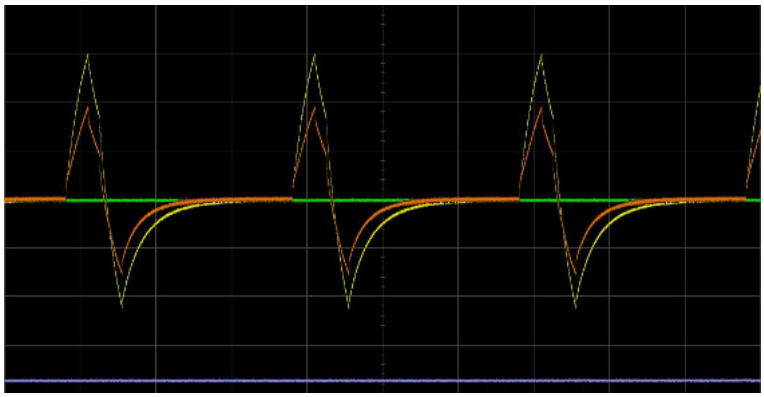

(b)

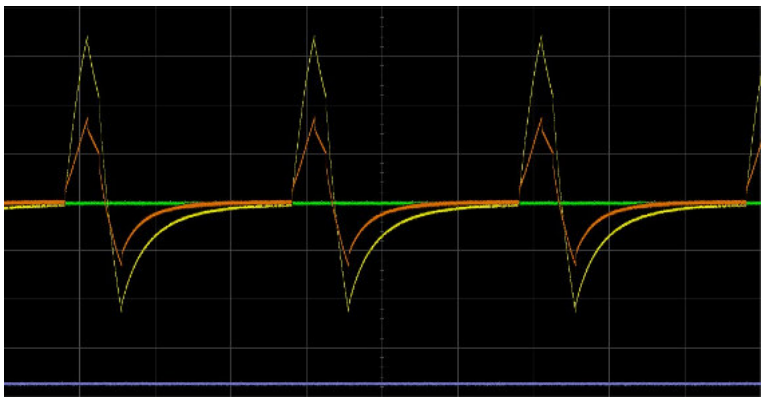

(c)

Figure 4.20: Voltage of the positive and negative output, trigger and stimulus currents measured at three different positions for a 50 kΩ to 100 kΩ electrode. Yellow: Voltage of the positive output (20 V per division), Green: Voltage of the negative output (20 V per division), Orange: Stimulus current (100 mV per division equivalent to 100 µA per division), Purple: Trigger (5 V per division), Time axis: 1 ms per division. Stimulus current measured at (a) the output, (b) the positive end, (c) the negative end.

tungsten wire			**electrode**		
	Vpp$^+$ [mV]	**%**		**Vpp$^+$ [mV]**	**%**
(1)	574	100	(1)	578	100
(2)	303	53	(2)	354	61
(3)	283	49	(3)	311	54

Table 4.11: Summary of Vpp^+ values obtained with the test microstimulation setup. Stimulus currents are measured as voltage differences at (1) the output, (2) the positive end, (3) the negative end with a tungsten wire and a microstimulation electrode. 1 mV are equal to 1 µA. % shows the percentage of the stimulus current with respect to its initial value provided at the output.

5 Discussion and outlook

In the following chapter all results obtained in Chapter 4 are discussed in Section 5.1. Then an outlook for the project is given in Section 5.2.

5.1 Discussion

Initially various systems for electrophysiological recordings and their measurement results obtained outside MRI environment are discussed in Subsection 5.1.1. Then in Subsection 5.1.2 the two different setup configurations based on the Tucker Davis system are compared and also discussed. Finally, in Subsection 5.1.3 a general discussion on the testing of the microstimulation device is given.

5.1.1 Outside MRI environment

Results obtained in Subsection 4.1.1, Subsection 4.1.2 and Subsection 4.1.3 are discussed and compared here. It can be summarized that the Tucker Davis system is the only one suitable for an fMRI extension or modification. The headstage is non-ferromagnetic and the pre-amplifier is fMRI compatible and additionally has a very large input range. The overall software is user-friendly and very powerful.

DAM80

The DAM80 differential amplifier provides a very inexpensive, fast option for broadband signal display on an additional device, i.e. an oscilloscope. However, the settings of this differential amplifier are only adjustable in a very limited range. The filters and amplification gain can be set to four different values which is not precise enough for most electrophysiological data recordings. Furthermore, no GUI is offered by the company WPI for a combined use with a data analysis software, i.e. Matlab. Nevertheless, it is used in several studies for doing electrophysiological recordings. In [20] responses of specific cells to electrical stimulation are observed using extracellular microelectrodes in combination with the DAM80. Signals are displayed on an oscilloscope and also transferred to a monitor. Also, physiological discharges in an animal brain model are measured in [15]. The recorded action potentials are amplified with the DAM80 which is coupled to an oscilloscope for display. These examples show that the DAM80 can certainly be used for some neurophysiological issues. However, for the given task of the development of an fMRI compatible setup this amplifier is not applicable. To sum up, it provides an initial characterization which forms the basis for a further analysis, i.e. in this study with the Open Ephys system.

Open Ephys

The Open Ephys platform provides a powerful open-source software for doing electrophysiological recordings. It is used by a huge number of research labs all over the world, all benefiting from shared development efforts and transparency software features. Its two biggest advantages are the low price and high flexibility for modification. This study shows that good SNR values can be achieved. The system definitely has a huge potential in neurophysiological recordings. Different setup configuration with respect to grounding and referencing are tested in this study. SNR values between 48.9 and 58.2 are achieved on the average. In the Open Ephys GUI signal characteristics such as amplitude, shape, etc. can be shown in much more detail than with an oscilloscope. However, when it comes to data acquisition and analysis the power of the system is limited. So far it is not possible to load pre-filtered data from the Open Ephys GUI into an analysis software i.e. Matlab. Therefore, time-consuming post-processing has to be done. In contrast to most commercial available recording systems Open Ephys does not a have a single record button, but requires at least one processor to the signal chain. Moreover, the documentation on the wiki platform is incomplete and support is very slowly provided as Open Ephys does not have full time employees. In this study the Open Ephys GUI has been observed to be unreliable during several acquisition sessions. As the software is developed by amateur engineers software bugs are present. Moreover, the modular architecture leads to a degree of overhead which results in decreased processing speed and a higher number of system crashes. Nevertheless, the awareness of Open Ephys is growing and a lot of research groups have already given the open-source project a try. A general introduction of the GUI is given in [50], in [23] the GUI is used to do high-density neural activity recordings with silicon probes and in [15] the acquisition board is used for doing electrophysiological recordings in animals with a ultradense probe, to name only a few applications.

An extension of the system to an MRI compatible version might be possible, but time-consuming. Here, a lot of effort has to be put into the hardware development as none of the components are MRI safe. The headstage would have to be changed to another compatible one, also an adapter to the electrode would have to be designed. A research group at the Harvard Medical School and the Massachusetts Institute of Technology developed a fully MRI compatible hardware and software acquisition for real-time electrophysiological recordings during fMRI scans in [45]. All of their software and hardware design files are available for free. They show that open-source based electrophysiological systems like the Open Ephys can be modified to an MRI safe version at low cost. However, they also point out the high development time and also that such complex system modification requires good knowledge in electronic circuit design and fabrication. Moreover, expertise in low-level microcontroller and high level LabView software skills are required. As such a complex modification of the Open Ephys system would have taken at least several months and due to the above mentioned reasons no further work was done with this system here.

Tucker Davis

The company Tucker Davis provides state-of-the-art neurophysiological research products. All of their hardware can be easily combined and the software Synapse meets the perfect spot between comfortable use, power and flexibility. It offers an intuitive environment for designing experiments. A greater variety of analysis tools than in the Open Ephys GUI is provided. Also, the technical support of this company is very transcendent. The Tucker Davis measurement setup developed within this study achieves a high SNR of 60.0 dB on the average.

The company Tucker Davis provides MRI compatible headstages and also a preamplifier that allows to record neurophysiological signals in the magnetic field. The three decisive reasons to use this system in the subsequent studies are: It provided the highest SNR values, the most user friendly software and MRI compatible equipment is available. Thus, only this system makes a low noise MRI compatible extension or modification possible.

Also, the research group of David Leopold, Ph.D. in the National Institute of Mental Health Information Resource Center is already using this system for monkey fMRI recordings with great results. The group is doing long-term recordings of single cells during fMRI in [32]. Additionally, they are using the same chronically implanted microelectrodes guided by fMRI targeting in [33].

5.1.2 Inside MRI environment

Results obtained in Subsection 3.2.1 and Subsection 3.2.2 are discussed below.

Broadband signal recordings

The initial approach of using a function generator to perform broadband signal recordings inside the scanner lead to good measurement results in the control room. The signal shape of the sine wave is clearly visible and as expected for all fundamental frequencies generated. Also, the amplitude spectrum shows an amplitude power at the applied fundamental frequency of around 50 times higher than the noise amplitudes, i.e. for the 60 Hz line noise component and its higher harmonics. Here, a simple Notch filter could be used to eliminate the 60 Hz noise. However, this would also diminish the useful signal in the adjacent frequency range. Another possibility to remove the line noise would be to set the differential acquisition mode instead of the single-sided one. The greatest advantage of the differential acquisition mode is that only the voltage difference between the signal and reference is measured. It is commonly used for the amplification of low voltage signals as it is independent of ground noise. No differences in the amplitude spectrum for the various fundamental frequencies are identified. Amplitudes of the various fundamental frequencies and the noise components are in a similar range for all measurements.

In a second step recordings are done inside the scanner. Again, 60 Hz line noise components and its harmonics are present in the amplitude spectrum. The amplitude spectrum also shows additional noise peaks in the low frequency range caused by the static magnetic field. To distinguish between randomly noise amplitudes and noise amplitudes caused by a specific device or condition all peak amplitude values

>0.10 µV are evaluated for all measurements. The complete list can be found in the Attachment. Noticeable is that especially in the range between 14 Hz to 60 Hz broadband noise could be verified across measurements. The most prominent peaks are at 41 Hz and 43 Hz. There are several studies that stated low frequency noise (<1 kHz) due to MRI scanner noise. One of the first research groups who investigated MRI acoustic noise levels are located at the Harvard Medical school. In [8] the group measures sound pressure levels with a microphone amplifier in the isocenter of five different MRI scanners and various pulse sequences. Fourier analysis shows broadband peaks in the low frequency range especially between 50 Hz and 1 kHz. Results of this study show that the magnetic field of the MRI scanner cause artefacts in the low frequency range which are dependent on several setting parameters, e.g. strength of magnetic field of the MRI scanner. Although the exact frequency positions of scanner induced noise does not match with this thesis, both show broadband low frequency noise caused by the static magnetic field. Variations in the exact position are primarily caused by the fact that different scanner models, parameter settings, etc. are used. In [42] artefacts in EEG recordings caused by the scanner environment are characterized. Data is recorded in two different 3.0 T Siemens Magnetom scanners with and without EPI sequences inducing the gradient switching artefact. As the scanner models magnetic field strengths applied in [42] are the same as in this thesis, reasonable comparisons can be made. Simultaneous EEG and fMRI measurements in [42] are performed on various subjects inside the scanner bore. Nierhaus et. al shows that the helium pump induces artefacts with broadband frequency power starting at 20 Hz or 30 Hz depending on the scanner model. Also the internal ventilation system of the scanner induces an artefact depending on the ventilation level and the scanner model due to vibration of the scanner interfering with EEG recordings. In [42] the artefact of the ventilation system is at 37 Hz, 41 Hz and 50 Hz (ventilation level 1, 2 or 3) and varied with ±1 Hz between the two scanners. Thus, the broadband signal noise in this study between 14 Hz and 60 Hz might also be caused by the helium pump of the scanner. The most prominent noise peaks are identified at 41 Hz and 43 Hz across all measurements. At this point it can be assumed that the ventilation level 2 of the Siemens Magnetom Prisma 3.0 T scanner lead to those frequency noise peaks. Both the broadband frequency noise due to the helium pump and also the ventilation system artefact are critical, as they lie in the physiologically relevant frequency range of LFP recordings. Although the artefact can be simply eliminated by switching off the scanner's ventilation system and thus enabling reliable acquisition of broadband signals, this is not recommended as discussed in Subsection 2.1.3. Also, in [4] noise induced by mechanical vibrations of the helium pump and the MRI room ventilation system in the low frequency range is verified. Although low frequency noise peaks observed in this study is in accordance with results in other studies, no definite explanation of every single peak can be given. As many reasons could have led to the low frequency noise amplitudes, no precise relationship between their occurrence and its reasons can be made at this point. As mentioned in Subsection 2.1.3 a variation in the loop area causes artefacts. In this thesis slight swinging of the cables needed to connect the amplifier to the headstage most likely caused additional severe artefacts. Also, the cable for connecting the headstage to the pre-amplifier could have picked up

noise. But not only equipment of the setup, also other devices in the room, such as lights might have caused noise in the data recordings. Thus, the testing of the equipment is highly recommended with a simpler signal source which is done in the following experiment.

In [2] the estimated induced maximal gradient artefact is ±250 mV for EEG-fMRI recordings. In this study the gradient artefact is even twice as high with around ±530 mV which exceeds the maximum input range of the pre-amplifier and thus causes its saturation. As a consequence there is no chance for this data set to be cleared of the artefact. The reason of the gradient artefacts is the switching magnetic field during the fMRI data acquisition and discussed in detail in Subsection 2.1.3. There are various studies for simultaneous EEG and fMRI recordings which are concerned with the optimal cable configuration. In [7] it is verified that twisted cables are better suited in the MRI environment due to the fact that the area of the loops sensitive to magnetic flux changes are minimized. In [4] it is further shown that shorter connection cables reduce the gradient artefact enormously.

In this thesis it is estimated that the cables which are used to connect the function generator to the headstage, are the main source of the induced gradient artefacts. First of all, they are not twisted and therefore produce a large loop area. Secondly, they are several meters long and thirdly no extra shielding is done. The setup could be improved by using fiber-optic cables for connection (as recommended in [1] for simultaneous EEG and fMRI setups) and by twisting the wires together. However, its length cannot be changed.

To sum up, low frequency noise components with no exact explanation are caused by the static magnetic field. The unchangeable long length of the wires for the connection of the function generator to the headstage is a main source of the gradient artefact and recordings during the fMRI scan cause saturation of the pre-amplifier. To exclude as many noise sources as possible and thus be able to make a more precise characterization, the measurement setup is simplified again. The next experiment is conducted with only a simple resistor as signal source in between the signal and reference channel of the headstage (see Subsection 3.2.2 for the materials and methods and Subsection 4.2.2 for the results).

Noise estimation

In this experiment the noise level of the system is evaluated in a first step and determined to be between ±75 µV, which is around three times as high as the noise level determined with the same system in Subsection 4.1.3. This can be explained by the fact that here no additional shielding of the headstage is done. No specific noise amplitude peaks are observed in the baseline measurements. However, a slightly higher amplitude with 0.012 µV is obtained at 0 Hz as AC coupling is used in the settings of the pre-amplifier. This DC offset could be eliminated by using DC coupling instead. Also, the line noise of 60 Hz is observed and could be eliminated with the connected drawbacks as discussed in Subsection 5.1.2.

For the measurements in the static magnetic field the RMS values and also the noise thresholds are increased only very minimally. However, frequency noise components are found additionally in the low frequency range in the amplitude spectrum

(see Fig. 4.15). As in Subsection 5.1.2 high amplitude values at 41 Hz and 43 Hz are found across all measurements. The quantity of the amplitude is reproducible over all noise estimation measurements, but do not match to the amplitude quantity observed in Subsection 5.1.2. The possible reasons are also discussed in Subsection 5.1.2. Again unspecific and unstable broadband frequency noise is observed which is most likely caused by the helium pump. In general, the helium pump artefact is found to be more unstable than the ventilation system artefact in this thesis. The amplitude peaks vary in quantity between the various measurements with this setup and compared to Subsection 5.1.2. This result is also found in [42] and [4] which both show an unstable broadband frequency artefact caused by the helium pump. All other noise amplitude peaks in the low frequency range might be because of the reasons already discussed in Subsection 5.1.2. In summary it can be stated that the ventilation system artefact caused a peak noise amplitude in all measurements done in the static magnetic field. Amplitude quantities are comparable within both experimental setups but not across them. The artefact caused by the helium pump causes broadband noise in the amplitude spectrum especially between 50 Hz to 100 Hz in both experimental setups. However, noise peaks in this frequency range are less stable. Neither amplitude quantification within the experimental setups nor across both setups can be shown. Also the exact position of the frequency varies. Finally, it can be said that noise sources are decreased in this setup compared to Subsection 5.1.2. However, it should be mentioned that also the connection wires of the resistor are minimally ferromagnetic and thus cause undesired interference with the magnetic fields.

In contrast to Subsection 5.1.2 the gradient artefact in this experimental setup does not cause saturation of the pre-amplifier which means that it could be removed by complex restoration schemes. There are several options for removing this periodical occurring artefact for simultaneous EEG and fMRI recordings mentioned in Subsection 2.1.3.

5.1.3 Microstimulation

We have shown that the stimulus currents are decreased in amplitude due to the long transfer distance from the control room in the scanner bore. Furthermore, the shape is changed due to capacitive properties of the cables. The result corresponds to [36]. Here it is also observed that only 50 % to 90 % of the original charge is finally delivered into the tissue. Subsequently, the capacitive properties of electrode and cable lead to an inverted current at the end of each rectangular half-pulse on the control oscilloscope. As the setup has been tested successfully, it can be used in a next step for the study of the connectivity of face patches in macaques by using combined electrical microstimulation and fMRI recordings.

5.2 Outlook

In this thesis a setup for simultaneous broadband signal recordings in an MRI environment is successfully developed and characterized. Also, a setup for microstimulation is tested. Nevertheless, many questions could not be answered sufficiently.

In the following recommendations for further steps on the project are given.

In a first step it is strongly recommended to further improve the experimental setup instrumentation configuration before spending time on artefact removal strategies or doing additional recordings. Initially, the positioning of the equipment in the scanner room of the experimental setup configuration in Subsection 3.2.2 should be optimized. In this study the pre-amplifier is positioned laterally to the patient trolley. Positioning the pre-amplifier on the patient trolley in a line to the isocenter of the scanner bore might result in noise reduced data sets as the magnetic field is homogeneous at this point. However, the virtually inexistent shielding on the inlet of the scanner bore compared to its sides might result in a higher magnetic field influence and thus eliminate the advantage of a homogeneous magnetic field interference. Another challenge is in the repositioning of the equipment are the predefined dimensions of the connection cables, i.e. fiber-optic and headstage cables.

After having optimized the positioning of the equipment, more considerations on the optimal shielding should be done. In this study the pre-amplifier is shielded with a Faraday cage. This reduced the electrical interference, however it is not effective against magnetic distortion of the device. In the future, magnetic shielding of the pre-amplifier should be tested. As mentioned in Subsection 2.1.4 the further magnetic shielding might cause magnetic field inhomogeneities which means that no improvement in data quality is guaranteed. It might also be necessary and result in noise reduced data if the headstage is also shielded. However, a solution must be considered so that the equipment can still be used for animal recordings. Additionally, an electromagnetic shielding of the iron connection wires attached to the ceramic resistor should be done. Although the iron connectors are very short and light-weighted, they might cause undesired field inhomogeneities.

Also, a better fixation of the various setup instrumentation parts, especially of the wires inside the MRI room should be done. In this way artefacts caused by movement of the equipment are minimized.

Optimization could be done on the settings of the pre-amplifier such as the system rate and filter parameters. For almost all of them a compromise between computational effort, data storage and accuracy should be found. Instead of AC coupling, the setting DC coupling should be used to reduce the DC offset in the data.

Following more precise statistics about occurrence of the noise amplitudes and its quantification over several measurements should be carried out. The aim at this point is to find out exactly which artefacts are reproducible over time, measurements and quantification and which are random. The more information is available about an artefact, the easier it is to develop a successful removal strategy which would subsequently be the next logic consideration related to the project.

A further step for the experimental configuration of Subsection 3.2.2 would be to use a dummy brained filled instead of the resistor. This arrangement would have the advantage that electrode properties in the static and dynamic magnetic field could also be investigated. However, one has to take into consideration that this more complex setup variation might cause additional artefacts due to induced currents in conductive materials of the electrodes and a larger necessary conductive loop which is sensitive to magnetic field alterations.

Once the experimental setup configuration of Subsection 3.2.2 has been optimized, noise amplitudes and quantities characterized and removal strategies developed, more work should be done on the experimental setup configurations in Subsection 3.2.1. Here, the wires used for connection of the function generator to the headstage should be twisted to minimize the conductive loop area and thus eliminate noise. Moreover, they should be better fixated to the patient trolley to reduce motion artefacts. Also, as mentioned in Subsection 5.1.2 the acquisition mode should be switched to differential. Thus, the line noise of 60 Hz will be eliminated as the system is floating.

In this study we recorded data from a sine wave with various fundamental frequencies. However, a sine wave is very different to a neural signal. In order to produce a more realistic scene, rectangular pulses with both polarities and varied duty cycles simulating spike activity should be used instead of the sine waves for broadband signal recordings.

The ultimate goal is the simultaneous use of microstimulation, electrophysiological microelectrode recordings and fMRI. Thus microstimulation of a specific region and its effect on distally connected brain areas could be studied by using fMRI. In addition, electrophysiological microelectrode recordings in the area of microstimulation or in the distally activated connected regions could provide further valuable insights in the physiology of single cells and local field potentials and their contribution to neural networks. Thus, new insights in neural networks could be gained and neural brain research revolutionized.

Bibliography

[1] *EEG - fMRI: Physiological Basis, Technique, and Applications*. Springer, 2009.

[2] P. J. Allen, O. Josephs, and R. Turner. A method for removing imaging artifact from continuous EEG recorded during functional MRI. *NeuroImage*, 12(2):230–239, aug 2000.

[3] P. J. Allen, G. Polizzi, K. Krakow, D. R. Fish, and L. Lemieux. Identification of EEG events in the MR scanner: The problem of pulse artifact and a method for its subtraction. *NeuroImage*, 8(3):229–239, oct 1998.

[4] S. Assecondi, C. Lavallee, P. Ferrari, and J. Jovicich. Length matters: Improved high field EEG–fMRI recordings using shorter EEG cables. *Journal of Neuroscience Methods*, 269:74–87, aug 2016.

[5] A. Belitski, A. Gretton, C. Magri, Y. Murayama, M. A. Montemurro, N. K. Logothetis, and S. Panzeri. Low-frequency local field potentials and spikes in primary visual cortex convey independent visual information. *Journal of Neuroscience*, 28(22):5696–5709, may 2008.

[6] A. A. Boulton, G. B. Baker, and C. H. Vanderwolf. *Neurophysiological Techniques, I*. Humana Press, sep 1990.

[7] M. E. H. Chowdhury, K. J. Mullinger, and R. Bowtell. Simultaneous EEG–fMRI: evaluating the effect of the cabling configuration on the gradient artefact. *Physics in Medicine and Biology*, 60(12):241–250, jun 2015.

[8] S. A. Counter, A. Olofsson, H. F. Grahn, and E. Borg. MRI acoustic noise: Sound pressure and frequency analysis. *Journal of Magnetic Resonance Imaging*, 7(3):606–611, may 1997.

[9] G. Dimitriadis, J. P. Neto, A. Aarts, A. Alexandru, M. Ballini, F. Battaglia, L. Calcaterra, F. David, R. Fiath, J. Frazao, J. P. Geerts, L. J. Gentet, N. V. Helleputte, T. Holzhammer, C. van Hoof, D. Horvath, G. Lopes, C. M. Lopez, E. Maris, A. Marques-Smith, G. Marton, B. L. McNaughton, D. Meszena, S. Mitra, S. Musa, H. Neves, J. Nogueira, G. A. Orban, F. Pothof, J. Putzeys, B. Raducanu, P. Ruther, T. Schroeder, W. Singer, P. Tiesinga, I. Ulbert, S. Wang, M. Welkenhuysen, and A. R. Kampff. Why not record from every channel with a cmos scanning probe? mar 2018.

[10] T. Eichele. Mining EEG–fMRI using independent component analysis. *International Journal of Psychophysiology*, 73(1):53–61, jul 2009.

[11] J. Felblinger, J. Slotboom, R. Kreis, B. Jung, and C. Boesch. Restoration of electrophysiological signals distorted by inductive effects of magnetic field gradients during MR sequences. *Magnetic Resonance in Medicine*, 41(4):715–721, apr 1999.

[12] G. H. Glover. Overview of functional magnetic resonance imaging. *Neurosurgery Clinics of North America*, 22(2):133–139, apr 2011.

[13] A. K. Golinska. Coherence function in biomedical signal processing: a short review of applications in neurology, cardiology and gynecology. *Studies in Logic, Grammar and Rhetoric*, 25(38):73–81, 2011.

[14] A. Grinvald and R. Hildesheim. VSDI: a new era in functional imaging of cortical dynamics. *Nature Reviews Neuroscience*, 5(11):874–885, nov 2004.

[15] H. C. Han, D. H. Lee, and J. M. Chung. Characteristics of ectopic discharges in a rat neuropathic pain model. *Pain*, 84(2):253–261, feb 2000.

[16] R. H. Hashemi. *MRI: The Basics*. Lippincott Williams & Wilkins, 2012.

[17] M. M. Heinricher. Principles of extracellular single-unit recording. In Z. Israel and K. J. Burchiel, editors, *Microelectrode Recording in Movement Disorder Surgery*. Georg Thieme Verlag, 2004.

[18] A. Hess, D. Stiller, T. Kaulisch, P. Heil, and H. Scheich. New insights into the hemodynamic blood oxygenation level-dependent response through combination of functional magnetic resonance imaging and optical recording in gerbil barrel cortex. *The Journal of Neuroscience*, 20(9):3328–3338, may 2000.

[19] J. Ives, S. Warach, F. Schmitt, R. Edelman, and D. Schomer. Monitoring the patient's EEG during echo planar MRI. *Electroencephalography and Clinical Neurophysiology*, 87(6):417–420, dec 1993.

[20] R. J. Jensen, O. R. Ziv, and J. F. Rizzo. Thresholds for activation of rabbit retinal ganglion cells with relatively large, extracellular microelectrodes. *Investigative Opthalmology & Visual Science*, 46(4):1486, apr 2005.

[21] J. Jorge, F. Grouiller, O. Ipek, R. Stoermer, C. M. Michel, P. Figueiredo, W. van der Zwaag, and R. Gruetter. Simultaneous EEG–fMRI at ultra-high field: Artifact prevention and safety assessment. *NeuroImage*, 105:132–144, jan 2015.

[22] JoVE Science Education Database. An Introduction to Neurophysiology. *Neuroscience*, 2018. JoVE, Cambridge, MA.

[23] J. J. Jun, N. A. Steinmetz, J. H. Siegle, D. J. Denman, M. Bauza, B. Barbarits, A. K. Lee, C. A. Anastassiou, A. Andrei, Ç. Aydın, M. Barbic, T. J. Blanche, V. Bonin, J. Couto, B. Dutta, S. L. Gratiy, D. A. Gutnisky, M. Häusser, B. Karsh, P. Ledochowitsch, C. M. Lopez, C. Mitelut, S. Musa, M. Okun, M. Pachitariu, J. Putzeys, P. D. Rich, C. Rossant, W. lung Sun, K. Svoboda,

M. Carandini, K. D. Harris, C. Koch, J. O'Keefe, and T. D. Harris. Fully integrated silicon probes for high-density recording of neural activity. *Nature*, 551(7679):232–236, nov 2017.

[24] E. R. Kandel, J. H. Schwartz, T. M. Jessell, S. A. Siegelbaum, and A. J. Hudspeth. *Principles of Neural Science, Fifth Edition (Principles of Neural Science (Kandel))*. McGraw-Hill Education / Medical, 2012.

[25] K. Krakow, P. Allen, M. Symms, L. Lemieux, O. Josephs, and D. Fish. EEG recording during fMRI experiments: Image quality. *Human Brain Mapping*, 10(1):10–15, may 2000.

[26] K. Krakow, F. G. Woermann, M. R. Symms, P. J. Allen, L. Lemieux, G. J. Barker, J. S. Duncan, and D. R. Fish. EEG-triggered functional MRI of interictal epileptiform activity in patients with partial seizures. *Brain*, 122(9):1679–1688, sep 1999.

[27] Y. Leclercq, E. Balteau, T. Dang-Vu, M. Schabus, A. Luxen, P. Maquet, and C. Phillips. Rejection of pulse related artefact (PRA) from continuous electroencephalographic (EEG) time series recorded during functional magnetic resonance imaging (fMRI) using constraint independent component analysis (cICA). *NeuroImage*, 44(3):679–691, feb 2009.

[28] N. K. Logothetis. The neural basis of the blood-oxygen-level-dependent functional magnetic resonance imaging signal. *Philosophical Transactions of the Royal Society B: Biological Sciences*, 357(1424):1003–1037, aug 2002.

[29] N. K. Logothetis, M. Augath, Y. Murayama, A. Rauch, F. Sultan, J. Goense, A. Oeltermann, and H. Merkle. The effects of electrical microstimulation on cortical signal propagation. *Nature Neuroscience*, 13(10):1283–1291, sep 2010.

[30] N. K. Logothetis, J. Pauls, M. Augath, T. Trinath, and A. Oeltermann. Neurophysiological investigation of the basis of the fMRI signal. *Nature*, 412(6843):150–157, jul 2001.

[31] A. Mazzoni, N. Logothetis, and S. Panzeri. Information content of local field potentials. In *Principles of Neural Coding*, pages 411–430. CRC Press, apr 2013.

[32] D. B. T. McMahon, I. V. Bondar, O. A. T. Afuwape, D. C. Ide, and D. A. Leopold. One month in the life of a neuron: longitudinal single-unit electrophysiology in the monkey visual system. *Journal of Neurophysiology*, 112(7):1748–1762, oct 2014.

[33] D. B. T. McMahon, A. P. Jones, I. V. Bondar, and D. A. Leopold. Face-selective neurons maintain consistent visual responses across months. *Proceedings of the National Academy of Sciences*, 111(22):8251–8256, may 2014.

[34] V. Menon and S. Crottaz-Herbette. Combined EEG and fMRI studies of human brain function. In *International Review of Neurobiology*, pages 291–321. Elsevier, 2005.

[35] V. Menon, J. M. Ford, K. O. Lim, G. H. Glover, and A. Pfefferbaum. Combined event-related fMRI and EEG evidence for temporal-parietal cortex activation during target detection. *NeuroReport*, 8(14):3029–3037, sep 1997.

[36] S. Moeller, W. A. Freiwald, and D. Y. Tsao. Patches with links: A unified system for processing faces in the macaque temporal lobe. *Science*, 320(5881):1355–1359, jun 2008.

[37] R. J. Morecraft, K. S. Stilwell-Morecraft, and W. R. Rossing. The motor cortex and facial expression: New insights from neuroscience. *The Neurologist*, 10(5):235–249, sep 2004.

[38] T. Murta, M. Leite, D. W. Carmichael, P. Figueiredo, and L. Lemieux. Electrophysiological correlates of the BOLD signal for EEG-informed fMRI. *Human Brain Mapping*, 36(1):391–414, oct 2014.

[39] J. Navajas, D. Y. Barsakcioglu, A. Eftekhar, A. Jackson, T. G. Constandinou, and R. Q. Quiroga. Minimum requirements for accurate and efficient real-time on-chip spike sorting. *Journal of Neuroscience Methods*, 230:51–64, jun 2014.

[40] I. Neuner, J. Arrubla, J. Felder, and N. J. Shah. Simultaneous EEG–fMRI acquisition at low, high and ultra-high magnetic fields up to 9.4T: Perspectives and challenges. *NeuroImage*, 102:71–79, nov 2014.

[41] R. Niazy, C. Beckmann, G. Iannetti, J. Brady, and S. Smith. Removal of FMRI environment artifacts from EEG data using optimal basis sets. *NeuroImage*, 28(3):720–737, nov 2005.

[42] T. Nierhaus, C. Gundlach, D. Goltz, S. D. Thiel, B. Pleger, and A. Villringer. Internal ventilation system of MR scanners induces specific EEG artifact during simultaneous EEG-fMRI. *NeuroImage*, 74:70–76, jul 2013.

[43] F. Pittau, F. Fahoum, R. Zelmann, F. Dubeau, and J. Gotman. Negative BOLD response to interictal epileptic discharges in focal epilepsy. *Brain Topography*, 26(4):627–640, jun 2013.

[44] E. Premereur, I. C. V. Dromme, M. C. Romero, W. Vanduffel, and P. Janssen. Effective connectivity of depth-structure–selective patches in the lateral bank of the macaque intraparietal sulcus. *PLOS Biology*, 13(2):1–20, feb 2015.

[45] P. L. Purdon, H. Millan, P. L. Fuller, and G. Bonmassar. An open-source hardware and software system for acquisition and real-time processing of electrophysiology during high field MRI. *Journal of Neuroscience Methods*, 175(2):165–186, nov 2008.

[46] P. Ritter and A. Villringer. Simultaneous EEG–fMRI. *Neuroscience & Biobehavioral Reviews*, 30(6):823–838, jan 2006.

[47] K. Rosenkranz and L. Lemieux. Present and future of simultaneous EEG-fMRI. *Magnetic Resonance Materials in Physics, Biology and Medicine*, 23(5-6):309–316, jan 2010.

[48] A. Sharott. Local field potential, methods of recording. In *Encyclopedia of Computational Neuroscience*, pages 1–3. Springer New York, 2014.

[49] A. Shmuel, M. Augath, A. Oeltermann, and N. K. Logothetis. Negative functional MRI response correlates with decreases in neuronal activity in monkey visual area v1. *Nature Neuroscience*, 9(4):569–577, mar 2006.

[50] J. H. Siegle, A. C. López, Y. A. Patel, K. Abramov, S. Ohayon, and J. Voigts. Open ephys: an open-source, plugin-based platform for multichannel electrophysiology. *Journal of Neural Engineering*, 14(4):1–13, jun 2017.

[51] J. H. Siegle and J. Voigts. Open ephys, 2010.

[52] J. Sijbers, I. Michiels, M. Verhoye, J. V. Audekerke, A. V. der Linden, and D. V. Dyck. Restoration of MR-induced artifacts in simultaneously recorded MR/EEG data. *Magnetic Resonance Imaging*, 17(9):1383–1391, nov 1999.

[53] A. S. Tolias, F. Sultan, M. Augath, A. Oeltermann, E. J. Tehovnik, P. H. Schiller, and N. K. Logothetis. Mapping cortical activity elicited with electrical microstimulation using fMRI in the macaque. *Neuron*, 48(6):901–911, dec 2005.

[54] Tucker Davis Technologies (TDT). *Synapse Manual*, 2018.

[55] Tucker Davis Technologies (TDT). *System 3 Manual*, 2018.

[56] M. Ullsperger and S. Debener. *Simultaneous EEG and fMRI: Recording, Analysis, and Application*. Oxford University Press, 2010.

[57] S. Ulmer and O. Jansen. *Fmri: Basics And Clinical Applications*. 2013.

[58] E. Underwood. Updated human brain map reveals nearly 100 new regions. *Science*, jul 2016.

[59] J. N. van der Meer, A. Pampel, E. J. V. Someren, J. R. Ramautar, Y. D. van der Werf, G. Gomez-Herrero, J. Lepsien, L. Hellrung, H. Hinrichs, H. E. Möller, and M. Walter. Carbon-wire loop based artifact correction outperforms post-processing EEG/fMRI corrections—a validation of a real-time simultaneous EEG/fMRI correction method. *NeuroImage*, 125:880–894, jan 2016.

[60] World Precision Instruments (WPI). *DAM80 differential amplifier*, 2018.

[61] M. Wu and X.-W. Bai. *Neural Information Processing. Models and Applications*, volume 20. Springer Berlin Heidelberg, 2010.

6 Attachments

	Peak amplitude [µV]				
Frequency [Hz]	10	100	500	1000	2000
1	0.11	ε	ε	ε	ε
4	0.89	ε	ε	0.11	ε
9	ε	ε	ε	ε	0.14
10	9.06	0.11	ε	0.17	ε
11	ε	ε	0.18	ε	ε
12	ε	ε	ε	0.99	1.10
14	**1.14**	**1.18**	**1.24**	**ε**	**0.87**
16	0.57	ε	ε	ε	ε
17	ε	0.37	ε	0.30	0.59
19	**1.02**	**ε**	**0.66**	**0.77**	**0.93**
21	**0.66**	**0.70**	**0.89**	**1.16**	**0.97**
24	**0.70**	**0.55**	**0.56**	**0.70**	**0.88**
26	**0.75**	**ε**	**0.69**	**0.58**	**0.67**
27	ε	1.07	ε	ε	ε
28	ε	ε	ε	ε	0.65
29	0.64	ε	0.42	0.45	ε
31	ε	ε	ε	0.28	ε
32	ε	0.17	ε	ε	ε
33	ε	ε	ε	0.17	ε
34	**0.22**	**0.19**	**0.28**	**ε**	**0.21**
36	ε	ε	0.20	ε	0.30
38	0.23	ε	0.14	ε	ε
39	ε	0.27	ε	ε	ε
41	**0.88**	**0.95**	**1.45**	**1.19**	**0.84**
43	**1.56**	**1.67**	**2.21**	**1.66**	**1.52**
46	ε	ε	0.57	0.45	0.31
48	ε	ε	ε	0.21	ε
49	0.39	0.28	0.41	ε	ε
50	ε	ε	ε	0.14	0.24
51	0.15	ε	ε	ε	ε
53	**ε**	**0.15**	**0.14**	**0.19**	**0.21**
55	ε	ε	ε	0.17	ε
57	**0.21**	**0.24**	**0.29**	**0.26**	**ε**
58	ε	ε	ε	ε	0.15
60	ε	0.18	0.13	ε	0.13

Table 6.1: Part I. Peak amplitudes >0.10 µV in the amplitude spectrum. An entry of ε means that either no peak is detected at the given frequency or that it is <0.10 µV. Frequencies that cause a peak >0.10 µV in four or more measurements are bold.

	Peak amplitude [µV]				
Frequency [Hz]	10	100	500	1000	2000
62	0.10	ε	ε	ε	0.13
65	ε	0.12	ε	ε	ε
66	ε	ε	ε	ε	0.13
100	ε	9.01	ε	ε	ε
119	ε	0.10	ε	ε	ε
500	ε	ε	9.30	ε	ε
540	ε	ε	ε	ε	0.10
660	**0.21**	**0.20**	**0.17**	**0.20**	**0.18**
720	**0.33**	**0.31**	**0.28**	**0.32**	**0.33**
840	**0.19**	**0.18**	**0.15**	**0.18**	**0.16**
900	0.10	0.10	ε	ε	0.10
1000	ε	ε	ε	9.07	ε
...	...	...	...	...	...
2000	ε	ε	ε	ε	9.27
...	...	...	...	...	...

Table 6.2: Part I. Peak amplitudes >0.10 µV in the amplitude spectrum. An entry of ε means that either no peak is detected at the given frequency or that it is <0.10 µV. Peaks between 1000 Hz and 2000 Hz and >2000 Hz are not listed. Frequencies that cause a peak >0.10 µV in four or more measurements are bold.

	Peak amplitude [nV]				
Frequency [Hz]	1	2	3	4	5
3	ε	ε	ε	ε	12.23
21	10.45	ε	ε	13.09	ε
22	ε	ε	ε	ε	14.80
24	ε	ε	11.02	12.31	ε
27	12.47	ε	ε	ε	ε
29	ε	ε	10.08	ε	ε
41	**12.23**	**11.10**	**11.97**	**11.30**	**16.24**
43	**16.29**	**25.89**	**26.24**	**24.67**	**23.80**
45	11.32	ε	10.04	ε	ε
46	ε	ε	ε	10.52	10.64
49	$\boldsymbol{\varepsilon}$	**16.74**	**18.66**	**15.88**	**16.14**
57	ε	ε	ε	ε	13.23
58	10.76	ε	12.58	ε	ε
60	10.88	ε	11.48	14.86	ε
72	ε	ε	ε	16.18	29.76
98	**13.13**	**15.06**	**12.01**	$\boldsymbol{\varepsilon}$	**12.17**
112	10.46	ε	ε	ε	ε
129	ε	10.92	ε	ε	ε
134	10.54	ε	ε	ε	ε
207	ε	ε	ε	ε	10.93
237	ε	ε	ε	10.37	ε
382	ε	ε	ε	ε	15.12
392	ε	11.97	ε	12.47	11.33
397	ε	ε	ε	ε	10.11
419	ε	ε	ε	ε	10.90
423	14.86	ε	ε	11.67	ε
424	ε	ε	10.46	ε	ε
426	ε	15.89	ε	ε	ε
427	11.59	ε	10.73	11.23	ε
428	ε	10.31	ε	ε	12.41
429	14.70	ε	13.19	ε	ε
430	ε	ε	ε	ε	22.05
431	ε	16.77	ε	ε	ε
432	19.18	ε	ε	ε	ε
433	ε	10.09	ε	ε	ε

Table 6.3: Part I. Peak amplitudes >10.00 nV in the amplitude spectrum for all measurements (1, 2, 3, 4 and 5). An entry of ε means that either no peak is, detected at the given frequency or that it is <10.00 nV. Frequencies that cause a peak >10.00 nV in four or more measurements are bold.

	Peak Amplitude [nV]				
Frequency [Hz]	1	2	3	4	5
439	ε	ε	10.29	ε	ε
443	ε	ε	10.24	ε	ε
465	ε	ε	10.11	ε	ε
469	ε	ε	11.32	11.02	ε
470	11.95	ε	ε	ε	ε
471	ε	ε	ε	ε	13.87
472	ε	ε	ε	11.28	ε
473	14.65	ε	11.52	ε	ε
474	ε	13.17	ε	15.24	ε
475	12.89	ε	20.11	ε	10.83
478	14.64	ε	12.95	21.22	ε
480	25.67	ε	11.51	ε	ε
481	ε	ε	ε	18.42	11.37
482	11.76	26.13	ε	ε	ε
483	ε	ε	11.11	11.99	ε
484	ε	26.67	ε	ε	ε
486	ε	ε	ε	ε	11.19
487	ε	19.54	ε	ε	ε
488	ε	ε	ε	ε	16.06
490	11.59	24.19	11.39	ε	ε
492	14.00	ε	ε	13.11	ε
496	23.07	26.70	10.90	ε	ε
498	13.31	ε	ε	ε	ε
499	ε	10.63	ε	ε	ε
500	ε	ε	11.14	ε	ε
501	18.25	15.07	ε	ε	ε
503	17.97	ε	ε	14.62	ε
505	19.73	16.25	ε	ε	ε
508	ε	17.44	ε	ε	ε
510	14.75	ε	ε	ε	ε
514	13.89	ε	ε	ε	ε
588	ε	17.45	ε	ε	ε
683	11.33	ε	10.08	ε	ε
...	...	...	...	...	...

Table 6.4: Part II. Peak amplitudes >10.00 nV in the amplitude spectrum for all measurements (1, 2, 3, 4 and 5). An entry of ε means that either no peak is detected at the given frequency or that it is <10.00 nV. Peak amplitudes at frequencies >1000 Hz are not shown. Frequencies that cause a peak >10.00 nV in four or more measurements are bold.